

# Understanding the current-voltage characteristics of industrial crystalline silicon solar cells by considering inhomogeneous current distributions

Invited Paper

O. BREITENSTEIN\*

Max Planck Institute of Microstructure Physics, 2 Weinberg, D-06120 Halle, Germany

*Solar cells made from multi- or mono-crystalline silicon wafers are the base of today's photovoltaics industry. These devices are essentially large-area semiconductor p-n junctions. Technically, solar cells have a relatively simple structure, and the theory of p-n junctions was established already decades ago. The generally accepted model for describing them is the so-called two-diode model. However, the current-voltage characteristics of industrial solar cells, particularly of that made from multi-crystalline silicon material, show significant deviations from established diode theory. These deviations regard the forward and the reverse dark characteristics as well as the relation between the illuminated characteristics to the dark ones. In the recent years it has been found that the characteristics of industrial solar cells can only be understood by taking into account local inhomogeneities of the dark current flow. Such inhomogeneities can be investigated by applying lock-in thermography techniques. Based on these and other investigations, meanwhile the basic properties of industrial silicon solar cells are well understood. This contribution reviews the most important experimental results leading to the present state of physical understanding of the dark and illuminated characteristics of multi-crystalline industrial solar cells. This analysis should be helpful for the continuing process of optimizing such cells for further increasing their energy conversion efficiency.*

**Keywords:** solar cells, silicon, current-voltage characteristics, efficiency, modelling.

## 1. Introduction

The photovoltaic generation of electric energy from solar irradiation energy by solar cells is an important part of the alternative energy concept, which aims to reduce global warming by replacing fossil energy sources by renewable ones. In 2011, solar cells with an accumulated power of more than 37 GW have been produced, from which 30.9% were based on mono-crystalline and the majority of 57% on multi-crystalline silicon material [1]. Hence, crystalline silicon cells are the workhorse of a multi-billion dollar photovoltaic (PV) industry. This is the oldest type of solar cells, starting in the 1950s with the first mono-crystalline solar cells made for space applications having an efficiency of about 6% [2]. Since then, by many years of continuous research and development, the efficiency of silicon solar cells has been improved to a record level of now 25% [3]. Solar cells have a relatively simple structure. They just consist of an electrically contacted large-area p-n junction, which is equipped with a top grid contact so that the semiconductor material can be illuminated. The operation principles of solar cells are well-known and are included in textbooks on semiconductor devices [4].

The widely accepted model electrically describing silicon solar cells is the so-called two-diode model, which will be discussed in the following Section. However, the current-

-voltage ( $I$ - $V$ ) characteristics of industrial silicon solar cells show significant deviations from the classical two-diode model predictions. This holds especially for cells made from multicrystalline material fabricated by the Bridgeman method, which contains high concentrations of crystal defects like grain boundaries, dislocations, and precipitates [5]. Even the characteristics of industrial mono-crystalline cells, which do not contain these crystal defects, deviate from the theoretical predictions. Particularly, the so-called depletion region recombination current or second diode current is usually several orders of magnitude larger than expected, and its ideality factor is significantly larger than the expected value of two. This non-ideal behaviour was observed already very early and tentatively attributed to the existence of metallic precipitates or other defects in the depletion region [6]. In that Ref. 6 it was already suspected that local leakage currents could be responsible for the non-ideal diode behaviour, and it was speculated that the edge region of a cell could significantly contribute to these non-ideal currents. Later on this non-ideal behaviour was attempted to be explained also under the assumption of a homogeneous current flow by attributing it to trap-assisted tunnelling [7,8]. However, in silicon solar cells the defect levels being responsible for this effect never could be identified. It was also attempted to explain the large ideality factors solely by the influence of the series resistance [9,10]. As it will be shown in Sect. 3.1, this explanation is not sufficient for interpreting large ideality factors in well-processed cells.

\* e-mail: breiten@mpi-halle.mpg.de

It has turned out that the key for a detailed understanding of the dark characteristics of solar cells is the spatially resolved mapping of the local current density of solar cells in the dark. Note that most textbooks on solar cells still generally assume that a solar cell behaves homogeneously [11,12]. Until 1994 there was no experimental technique available which could map the forward current of a solar cell with sufficient accuracy. In principle, the dark current can be mapped by infrared (IR) thermography [13]. However, since silicon is a good heat conductor, the thermal signals are generally weak, and the images appear blurred. Therefore, conventional IR thermography is only able to image breakdown currents under a reverse bias of several Volts, and the obtained spatial resolution is very poor (several mm, see Ref. 13). The first method enabling a sensitive imaging of the forward current with a good spatial resolution was the “Dynamic Precision Contact Thermography” (DPCT) method [14,15]. Here a very sensitive miniature temperature sensor was probing the cell surface point-by-point in contact mode, and in each position the cell bias was square-pulsed and the local surface temperature modulation was measured and evaluated over some periods according to the lock-in principle. This technique already reached a sensitivity in the 100  $\mu\text{K}$ -range (standard thermography: 20 to 100 mK), and, due to its dynamic nature, the spatial resolution was well below one mm. Its only limitation was its low speed; taking a 100×100 pixel image took several hours. Therefore, DPCT was later replaced by IR camera-based lock-in thermography (LIT). This technique was developed already before it was introduced to photovoltaics [16] and since then mainly used in non-destructive testing, hence for “looking below the surface of bodies” [17]. In the following LIT was also used for investigating local leakage currents in integrated circuits [18] and in solar cells [19]. Meanwhile, LIT is a widely used standard imaging method for characterizing solar cells, which is commercially available. Details to its basics, realization, and application are given in Ref. 20. Since the illuminated characteristics of a solar cell is closely related to its dark characteristics, LIT can even be used for performing a detailed local analysis of the efficiency of inhomogeneous solar cells [21,22]. In the last years, in addition to LIT, also camera-based electroluminescence and photoluminescence imaging methods have been developed for the local characterization of inhomogeneous solar cells. An overview over these methods and their comparison to LIT-based methods can be found in Ref. 23.

In this review, first the usually employed theory for interpreting the  $I$ - $V$  characteristics of solar cells will be reviewed, and the results will be compared to experimentally measured characteristics. This comparison will show the non-ideal character of the characteristics of industrial silicon solar cells. In the next Sect. 3 the five major fields are outlined, which show deviations to the established theory. These are depletion region recombination (second diode) current (Sect. 3.1), diffusion (first diode) current (Sect. 3.2), ohmic current contributions (Sect. 3.3), reverse

current (Sect. 3.4), and the relation between the dark and the illuminated characteristics (Sect. 3.5). In these Sections the most important experimental and theoretical results leading to the present state of understanding the characteristics of industrial silicon solar cells will be reviewed and discussed.

## 2. Theory vs. experiment

The usually taught theory of solar cells always assumes an electrically homogeneous cell. Its current density  $J$  is in ideal case described by the Shockley’s diode equation [24]

$$J(V) = J_0 \left( \exp \frac{eV}{kT} - 1 \right) - J_{sc}. \quad (1)$$

Here  $V$  is the applied bias voltage (in forward direction),  $e$  is the electron charge,  $kT$  is the thermal energy, and  $kT/e$  is the thermal voltage  $V_T$  (25.69 mV at 25°C).  $J_{sc}$  is the current density flowing at short-circuit condition under illumination. This term represents the photocurrent, which is (at least for silicon solar cells) independent of the bias  $V$ , whereas the first term in Eq. (1) represents the voltage-dependent dark current density. For a dark characteristic  $J_{sc} = 0$  holds. According to Eq. (1) the illuminated characteristic equals the dark characteristic, shifted in negative current direction by the photocurrent  $J_{sc}$ , which is a reverse current. This is known as the “superposition principle”. Equation (1) holds both in forward and in reverse diode polarity, the latter corresponding to negative values of  $V$ . Hence, under a reverse bias of several  $V_T$  in the dark ( $J_{sc} = 0$ ), the current density equals  $-J_0$ , independent of the magnitude of the bias  $V$ . Therefore,  $J_0$  is called the “saturation current density”. From Eq. (1), for  $J(V) = 0$  (open-circuit condition, the photocurrent is completely balanced by the dark forward current), the well-known expression for the open-circuit voltage  $V_{oc} = V_T \ln(J_{sc}/J_0)$  can be derived. This expression shows the influence of the dark characteristics on the efficiency parameters: The smaller the value of  $J_0$ , hence the smaller the dark current density of a solar cell, the higher is its value of the open-circuit voltage  $V_{oc}$  and thereby its efficiency. This is the reason why a detailed understanding of the dark characteristic of a solar cell is essential for obtaining a good efficiency.

Equation (1) is only an idealized description of a solar cell. In reality, in addition a series resistance  $R_s$  (given in units of  $\Omega \text{ cm}^2$ , if referred to the current density) and at least two more dark current components have to be considered, which are the depletion region recombination (second diode) current [25] and an ohmic shunt current caused by a parallel resistance  $R_p$  (often called shunt resistance  $R_{sh}$ , also given in units of  $\Omega \text{ cm}^2$ , if referred to the current density). This leads to the so-called two-diode model [4], where the first diode represents the “ideal” diode of Eq. (1), describing the so-called diffusion current or the first diode current, characterized by a saturation current density  $J_{01}$ , and the second diode is the so-called recombination or second diode

current, characterized by a saturation current density  $J_{02}$  and an ideality factor  $n_2$ . As it will be discussed below, the diffusion (first diode) current is due to recombination in the base and the emitter, including their surfaces, and the recombination (second diode) current is due to recombination within the depletion region. Altogether, according to the two-diode model, the current density of a solar cell is described by (see Ref. 4)

$$J(V) = J_{01} \left( \exp \frac{V - R_s J(V)}{V_T} - 1 \right) + J_{02} \left( \exp \frac{V - R_s J(V)}{n_2 V_T} - 1 \right) + \frac{V - R_s J(V)}{R_p} - J_{sc}. \quad (2)$$

The magnitude  $V - R_s J(V)$  is the “local voltage” directly at the p-n junction, which is the applied voltage  $V$  minus the voltage drop at the series resistance  $R_s$ . This series resistance is defined here “area-related” in units of  $\Omega \text{ cm}^2$ , see Sect. 3.5. The six parameters in Eq. (2), which govern the properties of the solar cell, are the two saturation current densities  $J_{01}$  and  $J_{02}$ , the ideality factor  $n_2$  of the recombination current, the series resistance  $R_s$ , the parallel resistance  $R_p$ , and the short-circuit current density  $J_{sc}$ .

Note that the current density  $J(V)$  is given only implicitly in Eq. (2), which complicates all computations. Therefore, in a limited bias range (usually between the maximum power point and  $V_{oc}$ ), Eq. (2) is often simplified to the empirical “one-diode” solar cell equation containing effective values for  $J_0$  and the ideality factor  $n$

$$J(V) = J_0^{eff} \left( \exp \frac{V}{n^{eff} V_T} - 1 \right) - J_{sc}. \quad (3)$$

In this equation the influence of ohmic and recombination (second diode) current contributions is contained in  $J_0^{eff}$  and  $n^{eff}$ . This effective ideality factor  $n^{eff}$  is that of the whole current and not only of the recombination current. If a real cell characteristic is fitted to Eq. (3) for each bias  $V$ , this leads to the bias-dependent ideality factor  $n(V)$ , which is very useful for analysing the conduction mechanism of solar cells, see Sect. 3.1.

At this point the physical meaning of the two diode terms in Eq. (2) should be illuminated in some more detail. Fig. 1 shows schematically the band structure of a p-n junction (a) in thermal equilibrium, (b) under reverse, and (c) under forward bias. The dashed line represents a deep SRH recombination centre governing the excess carrier lifetime in the p-region.

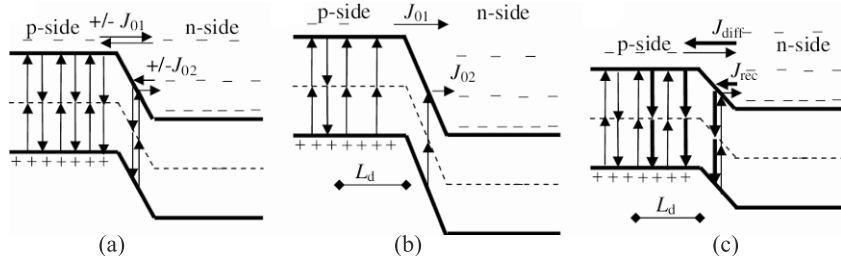


Fig. 1. Schematic band diagram of a p-n junction (a) in thermal equilibrium, (b) under reverse bias, and (c) under forward bias, only electron currents are shown. The dashed line represents a deep SRH recombination centre governing the excess carrier lifetime in the p-region.

under forward bias. The physics of a p-n junction can only be understood by considering horizontal and vertical thermally induced processes, which are symbolized in Fig. 1 by arrows. For clarity only electron processes are indicated, the same processes also hold for holes, where the energy scaling is inverted. Even in thermal equilibrium there is thermal generation (upward arrows) and recombination (downward arrows), and there is horizontal carrier movement. Note that the free carriers not only exist close to the band edges, as it is often displayed in such schemes, but also deep in the bands. They follow the Fermi statistics, which, if the Fermi level is lying within the band gap, corresponds to Maxwell-Boltzmann statistics. These electrons deep in the band are characterized by a large kinetic energy. Therefore, they may be called “hot” electrons, though they are in thermal equilibrium with all other electrons and with the lattice. With increasing energy distance  $\Delta E$  to the band edges, the free carrier concentration decreases essentially proportional to  $\exp(-\Delta E/kT)$ . Since the Fermi energy is going horizontally through Fig. 1(a) (not shown there), the concentration of electrons in the p-side (left) essentially equals that in the n-side (right) having an energy above the position of the conduction band edge in the p-side. Only these “hot” electrons have sufficient kinetic energy to overcome the decelerating electric field in the depletion region and to enter the p-side. The two driving forces for horizontal carrier movement are the concentration gradient, leading to the so-called diffusion current, and the electric field, leading to the field current. The consideration of these two current contributions independently, with only the sum of both being a measurable net current, is called the detailed balance principle. In thermal equilibrium, across the whole depletion region these two horizontal currents balance each other [4]. Then also the net horizontal current across the p-n junction is zero. A similar detailed balance principle holds for recombination and thermal generation. In any position, under thermal equilibrium, thermal carrier generation is balanced by carrier recombination. For any kind of homogeneous carrier generation, the equilibrium electron (minority carrier) concentration at the p-side  $n^p$  can be expressed by the generation rate  $G$  (given in units of generated carriers per  $\text{cm}^3$  and second) multiplied by the excess carrier lifetime  $\tau$ . This relation is the base of all quasi-static lifetime measurement techniques. It also holds for the equilibrium thermal carrier generation in the volume sketched in Fig. 1. On the other

hand, the electron concentration in the p-material can be expressed by  $n^p = n_i^2 / N_A$  ( $n_i$  = intrinsic carrier concentration,  $N_A$  acceptor concentration), leading to an expression for the thermal generation rate  $G$ :

$$n^p = G\tau = \frac{n_i^2}{N_A} \quad G = \frac{n_i^2}{\tau N_A}. \quad (4)$$

The interesting point here is why the equilibrium minority carrier concentration is independent of the lifetime: In regions of low lifetime the rate of carrier recombination is higher than elsewhere, but also the rate of carrier generation is higher.

Under reverse bias [Fig. 1(b)] the concentration of “hot” electrons at the n-side, which have sufficient kinetic energy to overcome the barrier, is reduced. Therefore, the diffusion current of electrons from the n- to the p-side becomes negligibly small. Now the current across the p-n junction is dominated by the diffusion of thermally generated electrons from the p-side to the n-side. The electric field of the junction drains all electrons generated within one diffusion length  $L_d = \sqrt{D_e \tau}$  ( $D_e$  = electron diffusion constant in the p-region). This horizontal current density, which is exactly  $J_{01}$  in Eq. (2), can be expressed regarding Eq. (4) as

$$J_{01} = GeL_d = \frac{en_i^2 L_d}{\tau N_A} = \frac{n_i^2 e \sqrt{D_e}}{N_A \sqrt{\tau}}. \quad (5)$$

Under zero bias, this field current is exactly balanced by the diffusion current of electrons running from the n- to the p-side, see Fig. 1(a). If a forward bias is applied [Fig. 1(c)], the magnitude of this diffusion current rises exponentially with increasing forward bias  $V$ , since correspondingly more electrons have enough kinetic energy to overcome the energy barrier. This finally leads to the first term in Eq. (2), which is traditionally called “diffusion current” for the reason described above, with the saturation current density [Eq. (5)]. These electrons recombine in the p-region basically within one diffusion length  $L_d$ , indicated by the thick downward arrows. This means that  $J_{01}$  is a measure of the bulk recombination rate within one diffusion length; the stronger the bulk recombination (low  $\tau$ ), the larger is  $J_{01}$ , and the smaller is  $V_{oc}$ .

The name “diffusion current” suggests that this current contribution were governed by transport properties, which is actually misleading. It is wrong to imagine the p-n junction as a kind of valve, where the magnitude of the current flow were only governed, e.g., by the barrier height. Instead, it must be considered that, both under zero and under forward bias, the lateral carrier exchange between n and p side due to the thermal carrier movement is so strong that the magnitude of the net current is determined by the speed at which the carriers are recombining on the other side. Therefore, in some research groups the first diode term in Eq. (2) is called “recombination current”, which is traditionally used for the second diode term in Eq. (2) [25], see below. This still increases the linguistic confusion. Therefore,

throughout this work the first diode current will be called “diffusion current”, and the second diode term “recombination current”, as historically introduced [25] and also used in textbooks [4]. The correct way to imagine the first diode current is to consider the quasi Fermi levels of electrons and holes as chemical potentials, which essentially horizontally cross the p-n junction, as it is described, e.g., by Würfel [12]. Then, it can easily be understood that each single recombination channel (e.g., bulk and surface recombination) leads to a separate and independent contribution to the corresponding total  $J_{01}$ . The same physics works for the hole exchange between the emitter and the base, which is not shown in Fig. 1, leading to  $J_{01}^e$  (“e” for emitter). Since the emitter (donor) doping concentration  $N_D$  in the denominator of Eq. (5) is very high, the emitter contribution of  $J_{01}$  is often neglected compared to the base contribution. It will be shown in Sect. 3.2. that this is not generally justified.

Equation (5) actually only holds for a cell having a thickness much larger than the minority carrier diffusion length in the material [4]. In reality the thickness of a well-processed solar cell is not large but rather small compared to the diffusion length. Then, also the recombination at the back surface and/or the back contact contributes significantly to the bulk recombination and, thus influences  $J_{01}$ . Other equations for  $J_{01}$ , which contain the influence of a finite bulk thickness and the upper and lower surface recombination velocities, can be found, e.g., in the appendix of the PVCDROM [26]. The use of these equations is often avoided by replacing  $\tau$  in Eq. (5) by an effective bulk lifetime  $\tau_{eff}$ , which also includes the back surface recombination. A typical average value for  $\tau_{eff}$  of a monocrystalline silicon solar cell in today’s standard technology implying a full-area Al back contact is about 160  $\mu$ s, and for a multicrystalline cell it is about 40  $\mu$ s, leading to expected values of the base contribution of  $J_{01}$  of about 500 and 1000 fA/cm<sup>2</sup>, respectively. It must be noted that the use of  $\tau_{eff}$  in combination with Eq. (5) is actually misleading. It suggests that the diffusion current were proportional to the inverse square root of the lifetime. For an infinitely thick cell this square root dependence only stems from the fact that the recombination volume is proportional to the diffusion length  $L_d \sim 1/\sqrt{\tau}$ . Within this volume, the recombination rate is proportional to  $1/\tau$ . In the same way, if the cell is thinner than  $L_d$  and the recombination volume is constant, the recombination rate and, thus also the diffusion current is proportional to  $1/\tau_{eff}$  and not to  $1/\sqrt{\tau_{eff}}$ .

As Fig. 1(c) shows, the diffusion current under forward bias consumes only the high energy fraction of the electrons in the n-side. Due to this current flow the temperature of the electron gas decreases, which instantly leads to a decrease of the crystal temperature. This is the physical reason for the Peltier cooling effect, which occurs at the p-n junction under forward bias [27].

The second diode term in Eq. (2) is due to recombination within the depletion region. This recombination is most effective for mid-gap levels and is then locally confined to a narrow region in the middle of the depletion region, where

in thermal equilibrium the Fermi level crosses the defect level [4]. The effective width of this region should be  $w$ . As Fig. 1(a) shows, at zero bias in this region recombination and thermal generation occur at the same time in the same place, as in the neutral material. However, they occur with a significantly higher rate per volume, since the electron occupancy state of the mid-gap level is 1/2 here, whereas in the neutral p material it is very small. Therefore, this current is often called “recombination-generation current” [25]. As explained above, in this sense also  $J_{01}$  is a “recombination-generation current” of the neutral material. Again, under reverse bias (Fig. 1b), for the depletion region current generation dominates over recombination, and under forward bias (Fig. 1c) recombination dominates over generation. The generation rate in the middle of the depletion region  $G^{dr}$  is calculated in analogy to Eq. (4) by replacing  $n_p$  by  $n_i$ . The saturation current density  $J_{02}$  is then calculated in analogy to Eq. (5), leading to

$$G^{dr} = \frac{n_i}{\tau} \quad J_{02} = G^{dr} ew = \frac{en_i w}{\tau}. \quad (6)$$

Under forward bias, the quasi Fermi energies in a silicon cell are usually horizontal across the p-n junction, therefore in any position of the junction  $np = n_i^2 \exp(V/V_T)$  holds. This recombination occurs in the middle of the depletion region, therefore in this region  $n = p = \sqrt{np} = n_i \exp(V/2V_T)$  holds. Since the recombination current is proportional to  $n$  resp.  $p$  in this region, this is the deeper reason for the ideality factor of  $n_2 = 2$  in the second term of Eq. (2), with  $J_{02}$  given by (6).

Unfortunately, the effective recombination layer width  $w$  is not exactly known. In fact, the occupancy state of the mid-gap level is strongly position-dependent, and the extension of the recombination-generation region also depends on the bias  $V$ . This is the reason why, even for a mid-gap level,  $n_2$  is expected to be slightly smaller than 2 [9,25,28]. In Ref. 9 the graph shown in Fig. 2 was published ( $J_{02}$  called  $J_{0DR}$  here), which is based on realistic numerical device simulations using the same assumption of a mid-gap level as done here. It shows that, for a bulk conductivity of  $\rho_{bulk} = 1.5 \Omega \text{ cm}$ , which is typical for solar cells, and for a lifetime of about 40  $\mu\text{s}$ , the expected value of  $J_{02}$  should be about  $5 \cdot 10^{-11} \text{ A/cm}^2$ . Note that this is still significantly larger than  $J_{01}$ , which is expected to be  $10^{-12} \text{ A/cm}^2$  here ( $1000 \text{ fA/cm}^2$ ). Therefore, at low forward bias, the recombination current always dominates over the diffusion current, but at higher forward bias the diffusion current dominates. In the absence of ohmic currents, the expected effective ideality factor at low voltages should be about two, and at higher voltages it should be unity, as long as the base stays in low-injection condition, hence as long as  $n \ll p$  holds there. The bias, at which this transition occurs, strongly depends on the magnitudes of  $J_{01}$  and  $J_{02}$ . In our case it is expected to be about 0.2 V. Hence, at the maximum power point of a solar cell, which typically is close to 0.5 V, the theoretically expected characteristics should not be influenced by the recombination current anymore.

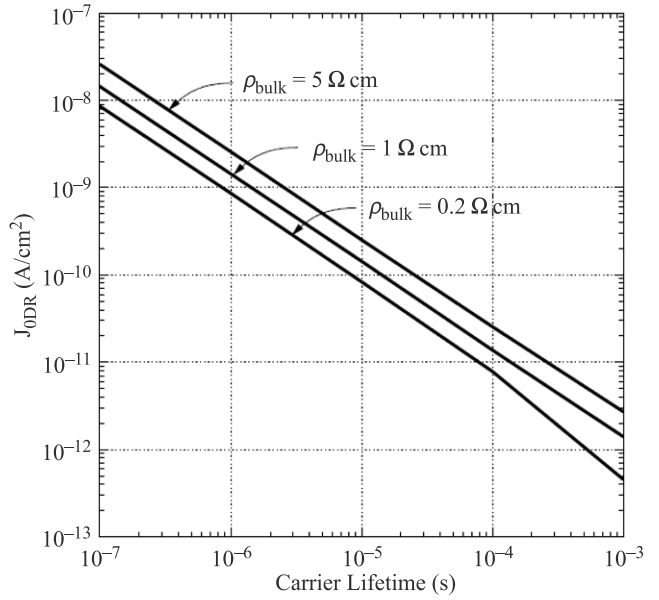


Fig. 2: Numerical simulation of a diffused silicon junction [9].  $J_{0DR}$  was only slightly affected by variation in the emitter profile (by kind permission of K.R. McIntosh).

The series resistance  $R_s$  in Eq. (2) contains contributions from the grid lines, from the contact resistances, from the horizontal current flow in the emitter layer, and from the current flow in the base. It will be shown in Sect. 3.5 that the use of a constant value for  $R_s$ , with the same value in the dark and under illumination, is actually wrong and represents only a coarse approximation. Nevertheless, this approximation is often made. Typical values for  $R_s$  are between 0.5 and  $1 \Omega \text{ cm}^2$ , see e.g. Ref. 7.

There is actually no established theory for an ohmic parallel resistance  $R_p$  across a p-n junction. However, experience shows that nearly all silicon solar cells show a significant amount of  $R_p$ , the reasons for this will be discussed in Sect. 3.3. Typical values of  $R_p$  are between some or some ten  $\Omega \text{ cm}^2$  (heavily shunted cells) and some  $10^4 \Omega \text{ cm}^2$  (faultless cells, see e.g. Ref. 7). Therefore, in most simulations  $R_p$  is externally added. An ideal solar cell, according to the diode theory described above, should have  $R_p = \infty$ , which is also assumed in the following theoretical simulations.

Note that, for correctly measuring  $R_p$  of a solar cell, the two-diode Eq. (2) has to be fitted to a measured dark or illuminated  $I$ - $V$  characteristics. It is not sufficient to evaluate only the linear part of the dark characteristics for low voltages and to interpret the slope as the inverse of  $R_p$ , as this is often being done. For low voltages, the two exponential terms in Eq. (2) may be developed in a power series. For small values of  $V$ , both lead to a linear characteristics near  $V = 0$ . For  $R_p = \infty$  the apparent (effective) parallel resistance is

$$R_p^{eff} = \frac{1}{\frac{J_{01}}{V_T} + \frac{J_{02}}{nV_T}} \approx \frac{nV_T}{J_{02}}. \quad (7)$$

The latter relation holds due to the fact that always  $J_{02} \gg J_{01}$  holds.

Under large reverse bias Eq. (2) is not valid anymore, since any p-n junction breaks down at a certain reverse bias. Moreover, since  $J_{02} \gg J_{01}$  holds, the thermal carrier generation in the depletion region governs the reverse current. For this case, the second exponential term in Eq. (2) is only an approximation. Under reverse bias, the generation region widens and becomes nearly homogeneous within the whole depletion width  $W$ , which increases with increasing reverse bias. Therefore, over a rather large bias range, as long as there is no avalanche multiplication yet, the reverse current  $J_r$  should increase according to Ref. 4.

$$J_r(V_r) = eG^{dr}W = \frac{en_iW}{\tau_p} = \frac{n_i\sqrt{2e\epsilon\epsilon_0(V_r + V_d)}}{\tau_p\sqrt{N_A}}. \quad (8)$$

Here  $V_r$  is the reverse bias as a positive number,  $\epsilon\epsilon_0$  is the permittivity of silicon,  $W$  is the depletion region width,  $V_d$  is the diffusion voltage of the junction (here about  $V_d = 0.9$  V), and  $\tau_p$  is the bulk lifetime in the p-region, which should be higher than  $\tau_{eff}$ , since it does not contain the back-side recombination. This means that, under reverse bias, the reverse current should increase sub-proportionally to  $V_r$ . If the electric field in the depletion region exceeds a certain limit, the carriers are multiplied by the avalanche effect, leading to a steep increase of the reverse current (breakdown). According to Miller [29] the avalanche multiplication factor can be described by

$$MC(V) = \frac{1}{1 - (V_r/V_b)^m}. \quad (9)$$

Here  $V_b$  is the breakdown voltage, and  $m$  is the Miller exponent, often assumed to be  $m = 3$ . For  $V_r = V_b$ ,  $MC = \infty$  holds, which is the basic definition of  $V_b$ . For a typical base doping concentration of  $10^{16}$  cm $^{-3}$  and a plane silicon junction,  $V_b$  is expected to be about 60 V [4,30]. Thus, the theoretically expected reverse current of a solar cell should be the product of Eqs. (8) and (9). Band-to-band tunnelling under reverse bias (internal field emission, Zener effect) should not play any role for silicon solar cells, since it dominates over avalanche multiplication only for a base doping concentration above  $5 \times 10^{17}$  cm $^{-3}$ , which is significantly higher than that used for typical solar cells [4]. However, trap-assisted tunnelling may be considered to be responsible for certain pre-breakdown phenomena, see Sect. 3.4.

Based on the theoretical predictions summarized above, now the theoretically expected dark and illuminated  $I-V$  characteristics of a typical multicrystalline solar cell with an effective bulk lifetime of 40  $\mu$ s may be calculated and compared with experimentally measured characteristics of a typical industrial cell. The results are presented in Fig. 3. This cell is a typical 156×156 mm $^2$  sized cell made in an industrial production line by the presently dominating cell technology (50  $\Omega$ /sqr emitter, acidic texturization, full-area Al back contact, 200  $\mu$ m thickness) from Bridgeman-type

multicrystalline solar-grade silicon material. The same cell is used for the comparison between dark and illuminated characteristic in Sect. 3.5. For calculating the theoretical illuminated characteristic, the value of  $J_{sc} = 33.1$  mA/cm $^2$  from the experimentally measured illuminated characteristic

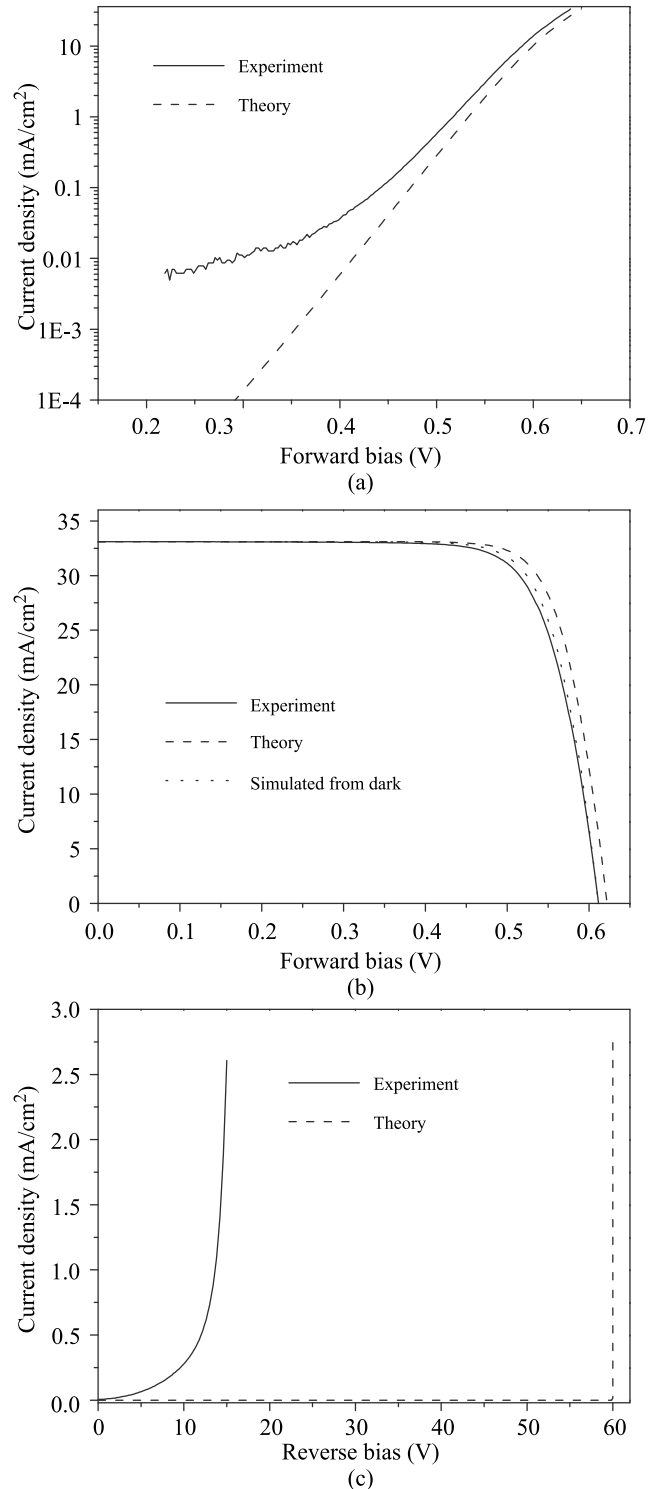


Fig. 3. Comparison of experimentally measured and theoretically predicted (a) dark forward, (b) illuminated, and (c) dark reverse  $I-V$  characteristics.

of this cell was used. The series resistance of  $R_s = 0.81 \Omega \text{cm}^2$  was calculated from the voltage difference between the measured open-circuit voltage (0.611 V) and the dark voltage necessary for a dark current equal to the short-circuit current (0.638 V). For the bulk lifetime in Eq. (8), as a lower limit the assumed effective bulk lifetime of 40  $\mu\text{s}$  was used.

It is visible in Fig. 3 that, in the dark forward characteristic (a), the low voltage range ( $V < 0.5$  V) shows the strongest deviation between theory and experiment. The measured current in this bias range is governed by the second diode and by ohmic shunting. In the theoretical curve there was no ohmic shunting assumed, and the second diode contribution is so small that it is not visible in the displayed data range. Also in the cell used for these characteristics the ohmic shunting is very low. It will be demonstrated in Sect. 3.5. that the shown experimental dark characteristic can be described by values of  $R_p = 44.4 \text{ k}\Omega \text{cm}^2$ ,  $J_{02} = 5.17 \cdot 10^{-8} \text{ A/cm}^2$  and  $n_2 = 2.76$ . Hence, there is non-negligible ohmic conductivity in this cell,  $J_{02}$  is several orders of magnitude larger than the predicted value of  $5 \cdot 10^{-11} \text{ A/cm}^2$ , and its ideality factor  $n_2$  is larger than the expected maximum value of two. The transition between the  $J_{02}$ - and the  $J_{01}$ -dominated part of the dark characteristic is close to the maximum power point near 0.5 V. This proves that in this cell the recombination current already influences the fill factor of this cell, even at full illumination intensity. This result is typical for industrial solar cells and has often been published, see e.g. Ref. 7. The reasons for these discrepancies to the theoretically expected behaviour will be discussed in Sects. 3.1 and 3.3. Also the experimental value of  $J_{01}$ , which governs the dark characteristic for  $V > 0.5$  V, is somewhat larger than theoretically expected. The reason for this discrepancy will be discussed in Sect. 3.2. Since the dark current was underestimated by theory, also the illuminated characteristic in Fig. 3(b) significantly deviates between theory and experiment. Both the open-circuit voltage  $V_{oc}$  and the fill factor are in reality smaller than theoretically estimated. This graph also contains the illuminated characteristic, which was simulated based on the experimental dark characteristic by applying the superposition principle and regarding a constant series resistance of  $0.81 \Omega \text{cm}^2$  both in the dark and under illumination. In this dotted curve  $V_{oc}$  is correctly described (it was used to calculate  $R_s$ ), but the simulated fill factor appears too large. This discrepancy will be resolved in Sect. 3.5. Finally, Fig. 3(c) shows the theoretical and experimental dark reverse characteristics. Also these curves deviate drastically. The theoretical dark current density is negligibly small for  $V_r < 50$  V (in the  $\text{nA/cm}^2$  range, sub-linearly increasing with  $V_r$ ), and the breakdown occurs sharply at  $V_r = 60$  V. In the experimentally measured curve, on the other hand, the reverse current increases linearly up to  $V_r = 5$  V and, then increases super-linearly, showing a typical “soft breakdown” behaviour. A sub-linear increase, as predicted by theory, is not visible at all. It will be outlined in Sect. 3.4 how this reverse characteristic can be understood.

In the following Sections the present state of understanding the different aspects of the non-ideal behaviour of industrial multicrystalline silicon solar cells, in particular of cells made from multicrystalline material, will be reviewed, and a selection of experimental results leading to this understanding will be presented. All results regarding the edge region or technological problems hold both for mono- and multi-crystalline cells. On the other hand, all results dealing with crystal lattice defects or precipitates only hold for multicrystalline cells.

### 3. Origins of non-ideal characteristics

#### 3.1. Depletion region recombination (second diode current)

It has been shown in the previous Section that, at full illumination intensity, the recombination current of a typical multicrystalline silicon solar cell influences maybe not its open-circuit voltage, but at least its fill factor and, thus its efficiency. This influence gets even stronger and also regards the open-circuit voltage, if the cell is operated at reduced illumination intensity, where all voltages become lower. Note that the yearly averaged energy yield of a solar panel, especially if operated in the middle Europe, strongly depends on its low light-level performance. It was already mentioned that several attempts were made before to explain the unexpectedly large recombination current and its unexpectedly large ideality factor. An ideality factor of the recombination larger than two means that, in the middle of the depletion region, the recombination current increases with increasing bias slower than proportional to the free carrier concentration, see the discussion to Fig. 1 in the previous Section. This means that, according to Eqs. (2) and (6), the lifetime  $\tau$  in the recombination region increases and  $J_{02}$  decreases with the increasing carrier concentration. This behaviour is called “saturation of a recombination channel”. While saturation of a SRH-type level usually leads to an S-shaped semi-logarithmic characteristics, an increased ideality factor over an extended bias range requires “gradual saturation”, which extends over many orders of magnitude of the carrier concentration, see next Section. It will be shown below that, for recombination in the depletion region, this gradual saturation may be explained by multi-level recombination at spatially extended defects.

Already Queisser [6] has discussed the contribution of the edge region to the current with a large ideality factor. Note that in the edge region of a solar cell the p-n junction crosses the surface, which always represents a region with a high local density of recombination-active gap states. This does not hold only if the edge is lying well-passivated below an oxide layer, as usual in the planar semiconductor technology. Thus, it can be expected that the edges of solar cells lead to a strong  $J_{02}$  contribution. To the knowledge of the author, the first direct hint that this is indeed the case for silicon cells was published in Ref. 31. Here a solar cell was successively divided into smaller pieces by diamond scrat-

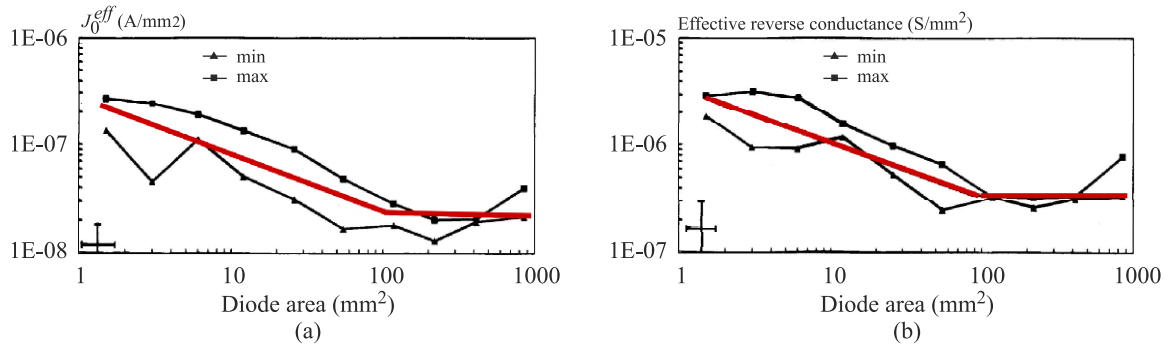


Fig. 4. Dark current data for solar cells with various areas based on Ref. 31, see text.

ching the backside and breaking, leading to cells with various areas differing by a factor of two. It was found that, for small cell sizes, both the forward and the reverse current was dominated by the edge current. The effective ideality factor increased with decreasing cell area from about 2.3 to 2.9. This points to the fact that, with decreasing cell area, the quantitative influence of the edge current increases, showing a large ideality factor. In a detailed evaluation of all cell pieces, which was not reproduced in Ref. 31, but was shown in the conference talk leading to this paper (Polyse Conference, San Malo, France 1993), dark  $I$ - $V$  characteristics of always two cell fractions having the same size were measured and evaluated according to Eq. (3), leading to two  $J_0^{eff}$ -values for each size. Also the reverse conductance  $G_p$  (the inverse of  $R_p$ , in units of  $S/mm^2$ ) was measured at about  $-1$  V for each cell fraction. From these results the dependencies of  $J_0^{eff}$  and  $G_p$  from the cell area  $A$  were obtained, which are shown in Fig. 4. The data show some scatter, therefore the images contain two experimental curves, one for the larger (max) and one for the smaller of the two values (min), the straight line is a guide for the eye. Over a wide area range towards small areas, both  $J_0^{eff}$  and  $G_p$  increase with  $1/\sqrt{A}$ , which is a clear proof that both the forward and the reverse current for small cell sizes are dominated by the edge current. Similar investigations (using cells with variable sizes or variable fractions of un-passivated edge) have been performed afterwards also by other authors, leading to similar results [9,32].

The degree of understanding of edge currents has decisively been improved by the results of surface scratching experiments, which were published first in Refs. 33 and 34. Here several  $1\text{ cm}^2$  sized high-efficiency PERL-type cells were used, which were fabricated in planar technology, hence their edges are well-passivated by an oxide layer. The original (virgin) dark characteristics of these cells all showed an ideality factor below 1.5 in the whole voltage range, and the reverse current was sub-linear in the nA-range. Hence, these cells behaved ideally in the sense of Sect. 2. The surface of these cells was flat. By using a diamond indenter and manual sample position movement, in three of these cells  $1\text{ mm}$  long scratches with different loads were made at the surface at room temperature in the middle between and parallel to two neighbouring grid lines.

Figure 5 shows the dark forward characteristics (a) and the voltage-dependent effective ideality factors (b) of these cells. The higher the scratch load, the stronger is the degree of non-ideality in the cells. Note that the  $I$ - $V$  characteristics in Fig. 5(a) look very similar to forward characteristics of the industrial cell shown in Fig. 3(a). Hence, diamond scratching at room temperature converts ideal cells into non-ideal ones. If the properties of small non-ideal cells are

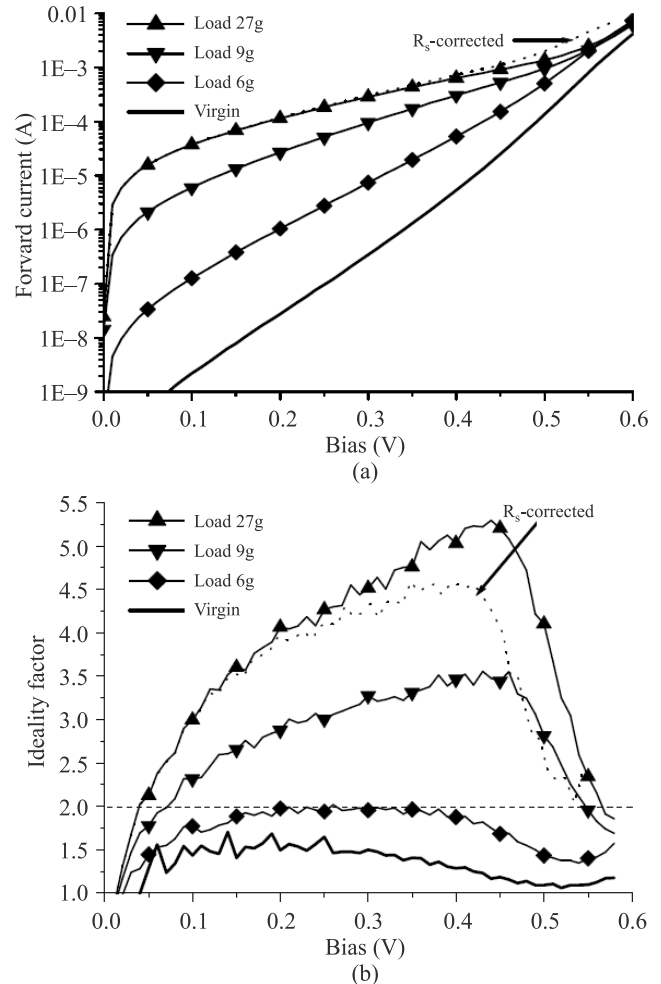


Fig. 5. (a) Dark forward characteristics and (b) voltage-dependent ideality factors of a virgin ideal solar cell (straight line) and three cells with  $1\text{ mm}$  long diamond scratches between grid lines with different loads, from Ref. 34.

governed by their edge region, this edge region obviously behaves similar to the scratches made here. Indeed, since the depth of the scratches, at least that with the higher loads, was above the junction depth, the scratch groove crossed the p-n junction, like the edge does. AFM imaging of the scratches revealed clear evidence of plastic deformation in the scratch region [34], hence the silicon material in this region was highly disturbed. While in the virgin cell the ideality factor is below 1.5 in the whole bias range, in the cell with the 6 g load scratch it increases up to 2, and for the higher loads it increases up to values of 5. It was suspected before these experiments that the actual edge still shows the ideality factor of 2, and that only the series resistance increases the ideality factor [9]. In our case, due to the simple geometry, the series resistance to the scratch can easily be calculated and corrected. Our emitter conductivity was  $100 \Omega/\text{sq}\mu$  and the scratch of 1 mm length was lying in the middle between two grid lines having a distance of 1 mm. Hence, the series resistance to this defect was the parallel circuit of two emitter regions of  $1 \cdot 0.5 \text{ mm}^2$  each, leading to a resistance of  $25 \Omega$ . This resistance could easily be corrected for the  $J_{02}$  contribution, leading to the dotted lines in Fig. 5. The result in Fig. 5(b) shows that, indeed, the series resistance further increases the effective ideality factor. However, this increase is only significant for higher currents above  $1 \text{ mA/cm}^2$ , and even the resistance-corrected curve shows an ideality factor well above 2 for currents down to the  $\mu\text{A}$ -range. This proves that the large ideality factor is an intrinsic property of a highly disturbed layer crossing the p-n junction. Obviously, the higher the degree of crystal disturbance (higher load), the larger are  $J_{02}$  and  $n_2$ . Similar experiments have been performed by exposing the p-n junction to laser cuts and cleaving along the (110)-direction [33]. The result was similar as in Fig. 4, except that the values of  $n_2$  were lower. For cleaving along (110) the maximum value of  $n_2$  was close to 2, and for laser cutting it was about 2.8. Obviously cleaving along (110) is the least disturbing kind of opening the p-n junction, leading to the lowest local density of recombination states. This explains why, for laboratory-type monocrystalline cells, where the edge is usually opened by cleaving along (110), often an ideality factor of 2 was measured for the recombination current. In this case the recombination still can be described by Shockley-Read-Hall (SRH) recombination statistics. This also seems to hold for the scratch with the lowest load, which did not penetrate the p-n junction yet. In this case obviously only point defects or dislocations, emitted from the scratch, influence the junction region. These results have been explained qualitatively already in Refs. 33 and 34, based on the coupled defect level recombination model of Schenk [8]. For a high local density of recombination states, recombination via multiple energy levels has to be considered, from which recombination across two levels is the simplest case.

In Fig. 6 different recombination models are summarized, (a) is the traditional Shockley-Read-Hall (SRH) point defect recombination model. In the original multi-level (actually two-level) recombination model of Schenk (b),

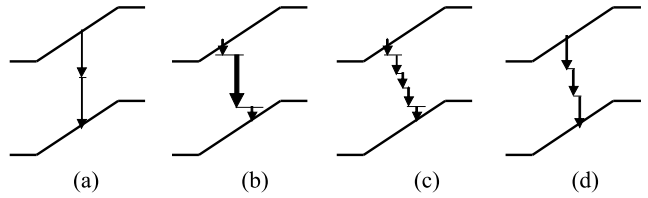


Fig. 6. Different models for depletion region recombination: (a) SRH model, (b) Schenk model, (c) multi-level model, (d) deep DAP model.

recombination via shallow and deep level or via two shallow levels was assumed, whereby the inter-level recombination probability was assumed to be infinite. The shallow levels are necessary here for explaining sufficiently high band-to-impurity tunnelling probability due to their spatially extended wave functions. The large ideality factor was explained in this model by the decreasing tunnelling probability to the shallow level with increasing forward bias due to the decreasing electric field strength. Since the inter-level recombination probability should depend exponentially on the inter-level distance, the assumption of a generally infinite probability is certainly not very realistic. Therefore, in Refs. 33 and 34 this model was further developed into the deep donor-acceptor-pair (DAP) recombination model. The main argument for this model came from the observed local character of the recombination current, which obviously only flows in the positions of extended defects. At these defects the local density of gap states should be extremely high. Therefore, the overlap of the wave functions even between deep levels should be sufficient for enabling significant inter-level charge transfer, which also may be called hopping. If the energy levels are spreading over the whole energy gap, the recombination model including inter-level charge transfer over multiple levels should look like in Fig. 6(c). However, this model is hard to calculate. Therefore, for investigating its principal properties, a recombination mechanism including only two deep levels was proposed, which is sketched in Fig. 6(d). It has been found in Refs. 33 and 34 that in this case the inter-level recombination is only more efficient than single level recombination and represents a significant additional recombination channel, if the levels show asymmetric capture coefficients, hence if they are of donor- and acceptor-type. Therefore, this model has been named “deep DAP” (donor-acceptor-pair) model. There are no restrictions as to the energy position of the two levels, hence the donor level may lay either above or below the acceptor level. In the latter case the inter-level transfer is thermally activated.

In this deep DAP model the high ideality factor is due to saturation of the inter-level recombination channel, leading to a hump in the  $n(V)$  characteristics. It was found that the magnitude and the position of this hump strongly depends on the energy positions and on the capture and inter-level recombination parameters of the two levels involved. Based on this qualitative model, recently a realistic quantitative model for describing high local densities of recombination

centres in depletion regions of p-n junctions has been introduced by Steingrube *et al.* [35]. In that work (Ref. 35), by using advanced 2-D device simulation techniques and realistic assumptions for the defect level distributions and recombination statistics, the experimental dark  $I$ - $V$  characteristics shown in Fig. 5(a) could be successfully reproduced. Moreover, electron injection from the emitter into a surface depletion layer of the p-region according to the model sketched in Fig. 7 was realistically simulated in Ref. 35, which was proposed already in Ref. 31 and also mentioned in Ref. 34. In Fig. 7 it is assumed that, due to the presence of surface states, only the surface of the low-doped p-region is depleted, but not that of the highly doped n<sup>+</sup>-region. It was found that this surface depletion provides indeed a second mechanism, independent of coupled defect level recombination, which may lead to currents with ideality factors larger than 2. By preferred injection of electrons into the depleted surface region of the p-material, this mechanism extends the effective recombination area, which otherwise was confined to the narrow line where the junction crosses the surface. Without this extension, the maximum possible value of the edge- $J_{02}$  would be limited by current crowding and the finite thermal velocity to some 10<sup>-8</sup> A/cm [36], whereas in reality values up to 10<sup>-5</sup> A/cm can be measured.

Thus, it can be assessed now that the physics behind unexpectedly large recombination currents showing unexpectedly large ideality factors seems to be clarified. This recombination current is flowing in local regions with a high density of recombination centres crossing the p-n junction. These regions may be the un-passivated cell edge or scratches or any other spatially extended highly recombination-active extended defects. The magnitude of this depletion region recombination current may be further increased by the field-induced extension of the surface recombination region sketched in Fig. 7. Hence, the recombination current is generally a local current and not a homogeneous one, therefore it cannot be explained by any 1-D cell model assuming homogeneous properties of the whole cell. This was proven by numerous dark lock-in thermography (DLIT) investigations published, e.g., in Refs. 14, 19, 20 and 21. Note that, at a relatively low forward bias of 0.5 V, the DLIT image is dominated by  $J_{02}$  contributions (recombination or second diode current), whereas at a higher forward bias of 0.6 V it is dominated by  $J_{01}$  contributions (diffusion or first diode current) [20].

If DLIT images taken at several biases are evaluated, the diffusion and recombination current contributions can be completely separated from each other [21]. In Fig. 8 such an image of the recombination current  $J_{rec}$  of a typical multi-crystalline cell measured at 0.55 V is shown [23], together with the image of the effective ideality factor between 0.525 and 0.55 V and an electroluminescence (EL) image of this cell, showing the distribution of the grown-in crystal defects in the bulk material. Note that, if  $n_2$  is taken as a variable, the local values of  $J_{02}$  spread over many orders of magnitude [22]. Therefore, it is useful to display the recombi-

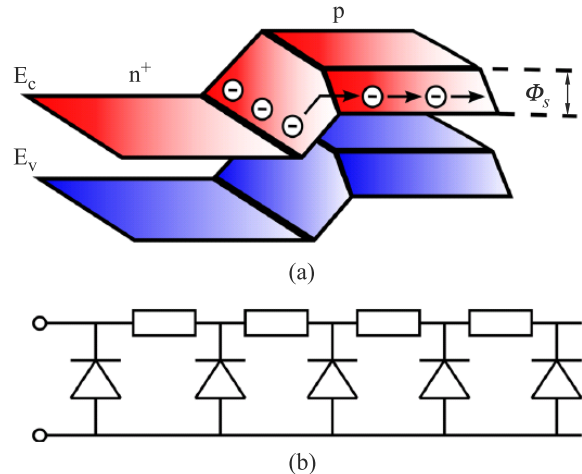


Fig. 7. (a) 2-D band diagram sketch, and (b) simplified equivalent circuit of recombination at the surface of the p-region close to the n<sup>+</sup>-p junction. According to this model, the surface recombination occurs in a larger region than in the small stripe where the p-n junction crosses the surface.

tion current density  $J_{rec}$  at a certain voltage instead of  $J_{02}$ . Only if  $n_2 = 2$  is assumed, the image of  $J_{02}$  is proportional to the local recombination current density. It is visible in Fig. 8 that the recombination current flows indeed only in some local positions, including the edge region, whereas in most of the area it is negligibly small. The circular shape of some of these " $J_{02}$ -type shunts" is an overexposure effect caused by the unavoidable thermal halo around each shunt; if properly scaled all these shunts would appear essentially point- or line-like. The effective ideality factor shown in Fig. 8(b) is close to unity in most of the area, including the crystal defect regions. In the edge region the effective ideality factor is close to  $n^{eff} = 2$ , but in some edge positions and especially in some local shunt positions it exceeds  $n^{eff} = 10$ . Since in these regions the recombination current dominates over the diffusion current, here  $n^{eff} = n_2$  holds. The spatial distribution of the recombination current is not visibly correlated to the distribution of the crystal defects visible in the EL image Fig. 8(c), in most of these defect regions  $J_{rec}$  is negligibly small. This, together with the not increased  $n^{eff}$  in the defect regions, proves that the bulk crystal defects do not significantly contribute to the recombination current. The nature of the distinct local maxima of  $J_{rec}$  in some spots in the area (so-called  $J_{02}$ -shunts) is not known yet.

Another argument for the validity of the above outlined theory of the recombination current is its striking similarity to the theory describing the  $I$ - $V$  characteristics of amorphous p-n junctions. According to Nardone *et al.* [37] these junctions are also characterized by a large ideality factor. The "optimal channel hopping" model described there actually corresponds to the multi-level model shown in Fig. 6(c). The hopping transport in amorphous material discussed by Nardone corresponds to the inter-level charge transfer discussed in our model. Amorphous material is equivalent to semiconductor material with a high density of gap states, as it may be present in un-passivated edge re-

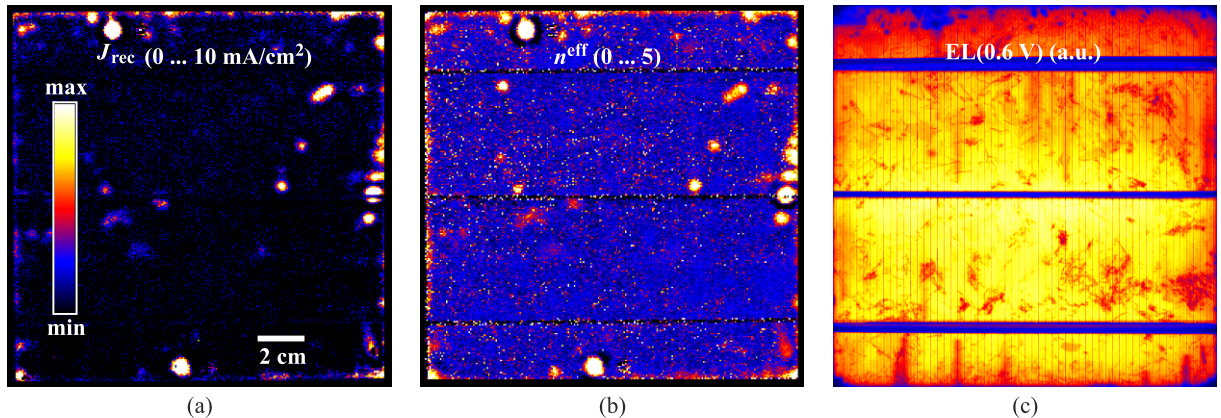


Fig. 8. (a) DLIT-based image of the recombination current of a multicrystalline silicon solar cell at 0.55 V and (b) of the effective ideality factor between 0.525 and 0.55 V, (c) EL image of this cell [a.u.], all taken from Ref. 23. The colour bar in (a) holds for all images, the scaling ranges are indicated in (a) and (b).

gions or at scratches. Indeed, it is well known from indenter experiments that plastic deformation of silicon in micro-regions may lead to the conversion of crystalline into amorphous silicon material. Nardone also described and explained the correlation between  $\ln(J_{02})$  and  $n_2$ , which is regularly experimentally observed by DLIT and also follows from our simulations [35].

### 3.2. The diffusion (first diode) current

Figure 9 shows an image of the diffusion current density of the cell used also for Fig. 8, again in comparison with the EL image [23]. Here the correlation is very good, the regions with locally increased diffusion current correspond to defect-containing regions with low EL signal. In these regions  $\tau_{\text{eff}}$  is reduced, leading according to Eq. (5) to a locally increased  $J_{01}$ . In this respect the diffusion current behaves as theoretically expected. The series resistance-induced vertical dark stripes in the EL image are not reflected in the DLIT image, since the latter is only linearly, but the EL image is exponentially dependent on the local voltage. However, it was shown in Sect. 2 that the mean value of  $J_{01}$  is somewhat larger than expected. This is due to the fact that,

for evaluating an inhomogeneous lifetime distribution in solar cell material, it is not permitted to average the local lifetime linearly, as it was assumed for the theoretical predictions in Sect. 2. Note that the dominant influence of the lifetime on solar cell efficiency is less its influence on  $J_{sc}$  but rather that on  $J_{01}$ . In a solar cell all regions are electrically connected to each other by the metal grid, hence all regions of the emitter are basically lying on the same electric potential. Hence, if  $J_{01}$  is distributed inhomogeneous, the value of  $J_{01}$  for the whole cell is in good approximation the linear average of  $J_{01}$  over all cell regions. Since according to Eq. (5)  $J_{01} \sim 1/\sqrt{\tau_{\text{eff}}}$  holds, this magnitude has to be averaged in an inhomogeneous cell for correctly estimating its efficiency according to a homogeneous cell model. This rule, which leads to a stronger emphasis of low lifetime regions, was first proposed by Sinton [38].

Note that the presence of the metal grid leads under illumination to the occurrence of lateral equilibrating currents in the cells, if the lifetime is inhomogeneous. Then, under open-circuit condition, the locally generated photocurrent  $J_{sc}$  only weakly depends on the local lifetime  $\tau$ , but  $J_{01}$  more strongly depends on it. Hence, since the bias is everywhere nearly the same, in “bad” regions of low lifetime or in some

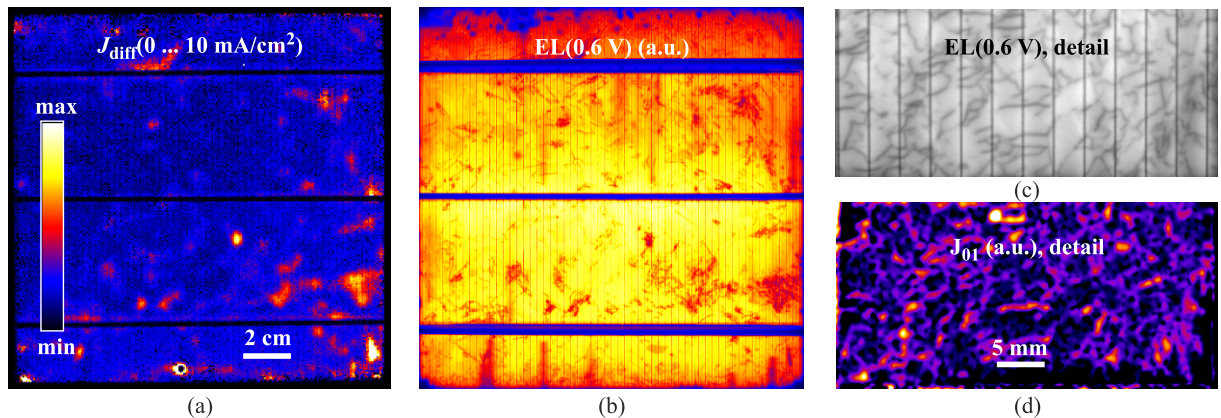


Fig. 9. (a) DLIT-based image of the diffusion current density of a multicrystalline silicon solar cell at 0.55 V and (b) EL image of this cell [a.u.], taken from Ref. 23, (c) EL image [a.u.], and (d)  $J_{01}$  image [a.u.] of a poor crystal quality region of an equivalent cell [39].

shunt positions there is a positive cell current and in “good” regions there is a negative one. With other words, the “good” regions generate net photocurrent, which is consumed by the “bad” regions as a dark current. Between these regions lateral equilibrating currents flow both in the bulk and in the emitter with its grid. Due to these currents, the minority carrier concentration in the “bad” regions is in a solar cell under illumination much higher than in an equivalent wafer, where these equilibrating currents do not flow. This has to be regarded e.g. for the interpretation of PL images of solar cells. Under maximum power point conditions these equilibrating currents become weaker, but still may exist.

While in the LIT-based diffusion current density image Fig. 9(a) of the cell, which was already used for Fig. 8, the regions with poor crystal quality appear quite homogeneous (cloudy), in the EL image (b) it becomes visible that they consist from narrow dark lines. These lines are recombination-active grain boundaries of various types. They become better visible in the higher resolution EL image [Fig. 9(c)] of a poor crystal quality region of another but equivalent solar cell [39]. Unfortunately, lock-in thermography, due to the inevitable lateral heat conductivity in silicon, does not allow to image such fine structures in its basic imaging mode. However, if the cell surface is covered by a thin black paint layer, a high lock-in frequency is used, and the thermal blurring is removed by spatial deconvolution, high-resolution LIT images leading to the result shown in Fig. 9 (d) may be obtained [39]. This image shows that also the bright regions in Fig. 9(a) actually consist from narrow bright lines on darker background. Hence, as also the EL image Fig. 9(c) shows, the lifetime in most parts of the multicrystalline material volume is quite good, but at the recombination-active grain boundaries it is considerably reduced. Therefore, in these grain boundary positions the local value of  $J_{01}$  is strongly increased, as Fig. 9(d) shows. Though these grain boundary regions occupy only a small fraction of the cell area, this leads to a significant increase of the average value of  $J_{01}$ , compared to that of the undisturbed material between the grain boundaries. It was estimated in Ref. 39 that, in this poor crystal quality region, about 60% of the current flows across the grain boundary regions and only 40% across the undisturbed area. Hence, by adding the grain boundaries to an undisturbed region, the average diffusion current increases by 150%. If we assume that the grain boundaries occupy about 10% of the area, in this region  $J_{01}$  must be increased, compared to the surrounding, by a factor of 15. Hence, according to Eq. (5), in this region the lifetime is reduced by a factor of  $15^2 = 225$ . Even if a linear dependence of  $J_{01}$  on  $\tau_{eff}$  is assumed, the local lifetime were reduced by a factor of 15 and the average by a factor of 1.5. If the lifetime were averaged linearly across this region, it would reduce by less than 10% due to the grain boundaries, leading according to Eq. (5) to only 5% increase of  $J_{01}$  (10% for  $J_{01} \sim 1/\tau_{eff}$ ). This has to be compared with the 150% increase of  $J_{01}$  in reality. This demonstrates that the inhomogeneity of the lifetime in multicrystalline material is the main reason why there the experi-

mental value of  $J_{01}$  of these cells is significantly higher than that expected from the linearly averaged effective lifetime of this material.

Another origin of non-ideal behaviour of the first diode current comes from an injection-level dependent effective lifetime. Shockley’s diode Eq. (1) only holds for a constant value of the excess carrier lifetime. If the Shockley-Read-Hall (SRH) capture coefficients of a recombination centre are asymmetric, hence if one of them is significantly smaller than the other one, the occupancy state of this centre may depend on the injection level [4]. This always leads to an increase of the lifetime with increasing injection level (i.e., with increasing minority carrier concentration), since the corresponding recombination channel tends to saturate. If only one SRH level should dominate the lifetime, this lifetime increases above a certain carrier concentration proportional to this concentration [40]. Also extended defects may lead to an increase of the lifetime with increasing injection level. The latter case usually holds for oxide-passivated back surfaces and also for electrically active grain boundaries or other extended crystal defects in multicrystalline material. Recombination rate saturation at oxidized surfaces has been analysed by Robinson *et al.* [41]. If the lifetime is governed by extended defects showing a high local density of states, these defects capture majority carriers and charge up, leading to a potential barrier with a depletion region around. It is well-known from deep level transient spectroscopy (DLTS) investigations that this type of extended defects does not show exponential carrier capture properties, as SRH-type point defect levels do, but rather a logarithmic “barrier-controlled” majority carrier capture and also non-exponential thermal emission [42]. Since, under steady-state injection condition, the majority carrier capture rate exponentially depends on the barrier height, this barrier height and the captured charge at the defect reduce logarithmically with increasing minority carrier concentration. This means that, in contrast to SRH-type levels, the saturation of the recombination of extended defects may occur slowly, extending over many orders of magnitude of carrier concentration.

According to Eq. (5) any increase of the effective lifetime leads to a reduction of  $J_{01}$ . Hence, any injection-dependent lifetime may be described by a voltage dependent saturation current density  $J_{01}(V)$ . If the lifetime variation occurs within a limited bias range, this leads to a hump in the dark  $I-V$  characteristics, hence in a limited forward bias region the ideality factor of the diffusion current is larger than unity. This has not to be confused with the depletion region recombination effects, that have been discussed in the previous Section. Such humps in the dark  $I-V$  characteristics have been found for recombination at oxidized surfaces [41] and for recombination dominated by a single SRH-level [43]. If the recombination is, however, dominated by extended crystal defects, like dislocations or grain boundaries in multicrystalline solar cells, the dark characteristics does not show a hump but, over a wide forward bias range, an ideality factor slightly larger than unity, as it was shown by

Macdonald *et al.* [40]. These authors have observed that the lifetime increases slower than expected for a single SRH level, and they explain this by the superposition of the action of two different SRH levels. An alternative and maybe even better explanation for the unexpectedly slow increase of the lifetime with carrier concentration would be to consider the special barrier-controlled recombination properties of this type of extended defects, as it was done for the interpretation of DLTS experiments [42].

If the saturation of the recombination activity can be described by  $n_1 > 1$  over an extended bias range, the two-diode equation reads

$$J(V) = J_{01}^{\#} \left( \exp \frac{V - R_s J(V)}{n_1 V_T} - 1 \right) + J_{02} \left( \exp \frac{V - R_s J(V)}{n_2 V_T} - 1 \right) + \frac{V - R_s J(V)}{R_P} - J_{sc}. \quad (10)$$

Here the saturation current density of the diffusion current is named  $J_{01}^{\#}$  for distinguishing it from  $J_{01}$  in Eq. (2). For  $n_1 > 1$ ,  $J_{01}^{\#}$  may be significantly larger than  $J_{01}$  at  $V = V_{mpp}$ . Hence, if  $n_1$  is considered as a variable, the values of the diffusion current density are quantitatively not comparable anymore with the  $J_{01}$  values obtained under the assumption of  $n_1 = 1$ . As mentioned above, the same holds for the recombination current density  $J_{02}$  if  $n_2$  is taken as a variable. An injection-level dependent lifetime can also be expressed in the conventional two-diode Eq. (2) by introducing a bias-dependent saturation current density of the shape [44]

$$J_{01}(V) = J_{01}^{\#} \exp \left[ \frac{V}{V_T} \left( \frac{1}{n_1} - 1 \right) \right]. \quad (11)$$

For  $n_1 = 1$ ,  $J_{01}^{\#} = J_{01}$  holds, and (2) and (10) become identical.

Note that it is hard to identify an ideality factor of the diffusion current larger than unity in a dark  $I$ - $V$  characteristic, if it occurs in addition to a strong recombination current with a variable ideality factor  $n_2$ . In a typical multicrystalline cell, the diffusion current dominates only in a small bias range, where the characteristic is also influenced by the series resistance. Therefore, in most analysis of  $I$ - $V$  characteristics, this effect will be attributed to variations of the other parameters. The more parameters are included in an  $I$ - $V$  characteristics' analysis, the less accurate are the results for each single parameter. Nevertheless,  $I$ - $V$  analysis have been made under the assumption of a variable  $n_1$ , and values significantly larger than unity have been obtained for cells made from multicrystalline material, in contrast to monocrystalline ones [7]. However, in this analysis the series resistance  $R_s$  is considered to be constant, which is also not correct, see Sect. 3.5. It will be shown in this Section that only the assumption of an ideality factor of the diffusion current larger than unity allows for a unified explanation both of the dark and the illuminated characteristics of multicrystalline solar cells with a consistent set of diode parameters, leading also to the correct value of the open-circuit voltage.

It was mentioned already in Sect. 2 that there are two different contributions to the saturation current, which are the base saturation current described by  $J_{01}^b$ , which is due to electron injection from the emitter into the base, and the emitter saturation current described by  $J_{01}^e$ , which is due to hole injection from the base into the emitter. The good correlation of  $J_{diff}$  to the bulk lifetime, which is reflected in the EL image shown in Fig. 9, is a strong indication that, at least in this case,  $J_{01}^b$  dominates over  $J_{01}^e$ . Note that the emitter of industrial silicon cells is highly doped up to  $10^{20} \text{ cm}^{-3}$ . In this doping range Auger recombination dominates, leading to a lifetime decreasing with the inverse square of the carrier concentration [4]. The emitter lifetime is further reduced by surface recombination, texturing, and diffusion-induced crystal defects [45]. Therefore, in spite of the high doping concentration,  $J_{01}^e$  may assume non-negligible values. Moreover, injection into the emitter is further enhanced by carrier-induced gap shrinking [46]. All these effects are independent of the existence of bulk crystal defects. It can, therefore, be expected that  $J_{01}^e$  is essentially homogeneous also in multicrystalline cells, though this has not been proven yet. While typical values of  $J_{01}$  for multicrystalline cells are between 1000 and 2000 fA/cm<sup>2</sup>, in the high-quality parts of industrial multicrystalline cells  $J_{01}$  was estimated to about 500 fA/cm<sup>2</sup> [39], which is about the value expected for monocrystalline cells of the present standard technology. Measured values of  $J_{01}^e$  on high-quality floating zone (FZ) material have revealed values between 20 and 200 fA/cm<sup>2</sup> [47]. Thus, for mono- and multicrystalline solar cells made by the presently dominating technology implying full-area Al back contact,  $J_{01}$  is not yet or only little influenced by  $J_{01}^e$ . In near future, however, also industrial solar cells will show high efficiency designs, implying dielectric backside passivation and lower doped emitters, where  $J_{01}^b$  may come into the 10 fA/cm<sup>2</sup> range. Then, for obtaining sufficiently high values of the open-circuit voltage  $V_{oc}$ , also  $J_{01}^e$  has to be minimized. Indeed, the present development goes into the direction of reducing the emitter doping concentration, which not only increases  $V_{oc}$  by reducing  $J_{01}^e$  (due to a higher effective emitter lifetime) but also by increasing  $J_{sc}$  due to a better blue-sensitivity of the cells.

### 3.3. The ohmic current

Ohmic shunts can easily be identified by DLIT, since they show the same thermal signal under forward and reverse bias, e.g., at  $\pm 0.5$  V [48]. The classical diode theory [24, 25] does not explain any ohmic conductivity. Many ohmic shunts have obvious technological origins, like an incompletely opened edge or a crack in the bulk material, where the emitter or some metallization paste crosses the cell [48]. Another very common type of ohmic shunts is caused by Al particles or residues of Al paste at the surface of the emitter. At the final contact firing step, this Al alloys in, leading to a p<sup>+</sup>-doped region around the particle by over-compensating the emitter. This p<sup>+</sup> region, which is in direct contact to the n-base, makes an ohmic tunnel junction to the n<sup>+</sup> emitter

region around, leading to the ohmic shunt [48]. These technology-originated shunts are well-known and will not further be described here.

The most common material-induced ohmic shunts in multicrystalline silicon material are due to filaments consisting from cubic SiC, having some  $\mu\text{m}$  diameter and hundreds of  $\mu\text{m}$  length, which are crossing the bulk material and short-circuit the emitter to the back contact [49,50]. These filaments develop preferentially in the upper part of the Si block due to oversaturation of carbon in the melt, and they preferentially grow within grain boundaries in growth direction. If a solar cell or a wafer is polished from both sides and imaged in a light microscope in transmission mode by using a black-and-white silicon CCD camera (without IR filter), the SiC filaments can be imaged as shown in the left part of Fig.10 (a) [50]. These filaments in a grain boundary, which are basically aligned in the direction of crystallization, perpendicular to the plane of Fig. 10(a), are usually branching and appear like a fence, where the varying inclination of the grain boundary to the surface governs the apparent width of the fence in the image. This figure also shows at the right some horizontally growing SiC filaments, which are not lying in a grain boundary. If the surface of a region containing such filaments is etched by HF-HNO<sub>3</sub>, the filaments stick out of the surface, as shown in Fig. 10(b) [50]. It has been found that these filaments are highly n-type doped by nitrogen, which is the dominant shallow donor in SiC and is present in the Si melt in high concentration [50,51]. Thus, if these filaments cross the cell, they are in direct electric contact to the n<sup>+</sup>-type emitter and yield a hetero-junction to the p-type base material. Therefore, these filaments can easily be detected by EBIC from the cell backside after removing the ohmic back contact [51]. If the filaments have also an ohmic connection to the base contact of the cell, they yield an ohmic shunt between the emitter and the base. A single SiC filament shows a typical resistance of several 100  $\Omega$  [51], but these filaments usually appear in groups counting many filaments, which leads to a serious shunting activity [48].

In monocrystalline silicon material there are no SiC precipitates, and in a technologically faultless cell also the other mentioned ohmic shunt sources should be absent. Nevertheless, even there the analysis of the dark I-V characteristics always reveals a certain amount of ohmic conductivity. Also here the investigation of diamond-scratched PERL-type cells has led to decisive progress in understanding this phenomenon. Fig. 11(a) shows the reverse characteristics of the cells diamond scratched at different loads [34], from which the forward characteristics were already shown in Fig. 5 in Sect. 3.1. While, in this scaling range, the reverse current of the virgin cell and that of the cell scratched at a load of 6 g (where the scratch did not penetrate the p-n junction yet) are negligibly small, the reverse current increases dramatically if the scratch penetrates the junction (loads of 9 and 27 g). This shows that scratching not only generates a strong  $J_{02}$  contribution, as shown in Fig. 5 of Sect. 3.1, but it also generates a significant ohmic current

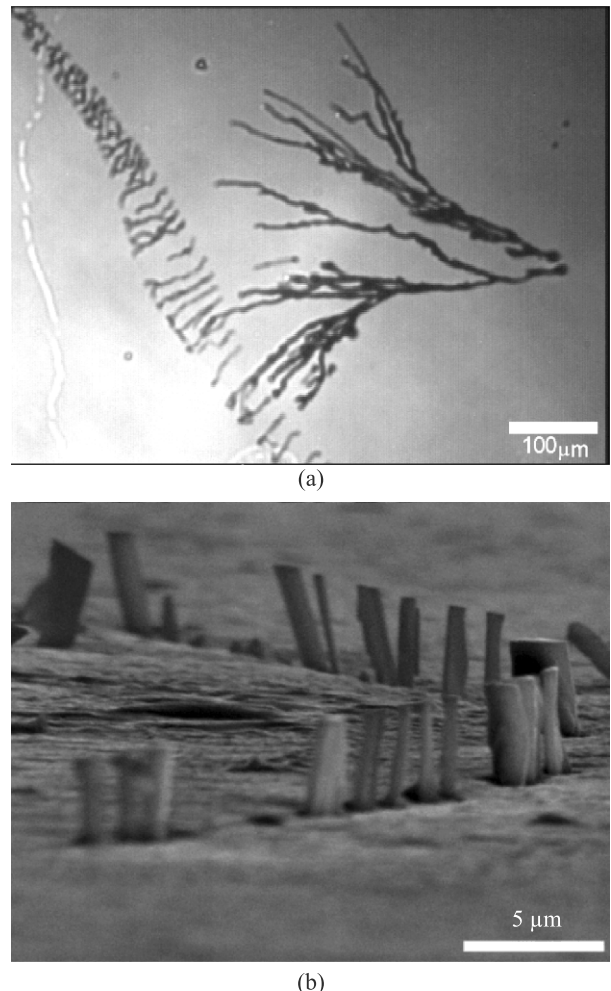


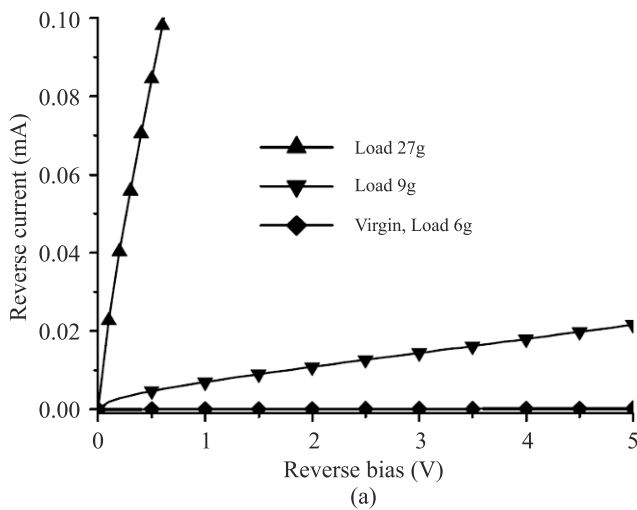
Fig. 10. (a) Light microscope image of SiC filaments in a polished wafer, (b) SEM image of SiC filaments sticking out of the surface after chemical surface etching.

contribution. For investigating the physical nature of this current, its temperature dependence was measured. In Fig.11(b) [34] the result is shown as  $\log(I)$  over  $1/T^{1/4}$ . It is visible that, in a wide temperature range from -50 to +100°C,  $\log(I)$  is proportional to  $1/T^{1/4}$ . This special temperature dependence is typical for variable range hopping conduction in a constant density of states near the Fermi level according to Mott's theory [52]. This type of conduction has been observed regularly for highly disturbed semiconductors and insulators, like nano- and microcrystalline silicon layers [53]. Hence, if the diamond scratching has generated a locally homogeneous and energetically continuous density of gap states, the hopping conduction mechanism at weak reverse bias may be sketched as in Fig. 11(c). Note that this mechanism corresponds exactly to the multi-level recombination mechanism sketched for the forward bias case in Fig. 6(c). Hence, if the local density of gap states is sufficiently high in some extended defects, under forward bias this causes multi-level recombination leading to an exponential characteristics with a large ideality factor. Under reverse bias it leads to a hopping conduction, which

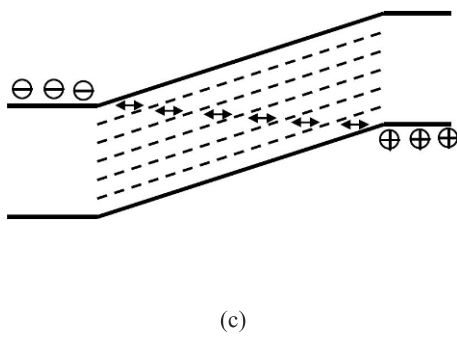
is ohmic for low reverse biases. These two processes are two sides of the same medal. This ohmic hopping conduction mechanism should also hold for non-passivated solar cell edges, and it explains the ohmic reverse conductivity of otherwise faultless industrial crystalline solar cells. The influence of the edge on the ohmic conductivity was proven also by the area-dependent reverse conductance shown in Fig. 4(b). A direct imaging of this edge current in another monocrystalline cell, which shows a very faint signal (see arrows), is shown in Fig. 11(d). In this image also leakage currents below the busbars are visible. For these, usually non-linear, shunts below the metallization, usually Schottky-type defects are made responsible [48]. Hence, it is assumed that there the metal is in a direct contact to the base. An alternative explanation were the in-diffusion of some metallic impurities from the metal paste into the underlying material. These impurities may generate a high local density of gap states in the depletion region, which may lead to depletion region recombination ( $J_{02}$ ), hopping conduction, or trap-assisted tunnelling, see next Section.

In 2009, Wagner *et al.* have introduced DLIT results pointing to a further ohmic conduction mechanism in multicrystalline silicon solar cells [54], which was unknown

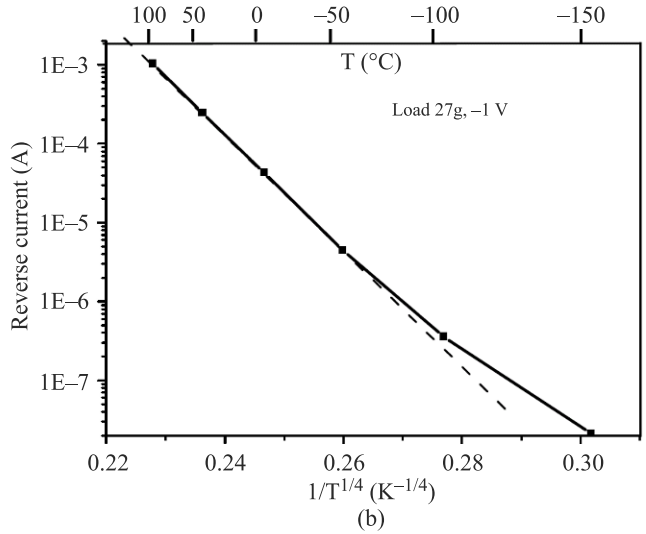
before and was described in more detail by Bauer [55]. Figure 12 shows DLIT-based current density images of an industrial multicrystalline cell at different temperatures, all measured at  $-10\text{ V}$  and displayed in the same sensitive scaling range [55]. The white regions in these images are the pre-breakdown sites, which will be discussed in Sect. 3.4. Here the interesting region is the area between the breakdown sites. The essentially homogeneous current density signal in this region clearly increases with increasing temperature. A detailed voltage- and temperature-dependent analysis of the region framed in Fig. 12 has revealed that the current in this region increases linearly up to  $-10\text{ V}$  and then reaches a kind of saturation. The temperature coefficient is a few  $\text{%/K}$  at room temperature and reduces with increasing temperature [55]. Until now, this current contribution has been found only in multicrystalline cells, but not in monocrystalline ones. The nature of this current contribution is not clear yet. It appears unlikely that this is  $J_{01}$  or  $J_{02}$  according to classical diode theory, since this current should be smaller by some orders of magnitude, it should show another temperature dependence, and it should correlate with the local defect density. According to Fig. 12, however, this current contribution seems to be nearly homoge-



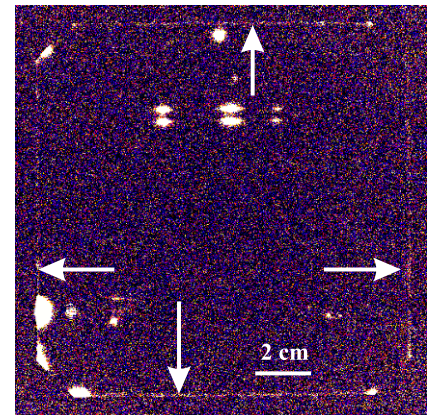
(a)



(c)



(b)



(d)

Fig. 11. (a) Reverse characteristics of the diamond-scratched cells of Fig. 5 [34], (b) temperature dependence of the reverse current at  $-1\text{ V}$  of the 27g loaded cell [34], (c) hopping conduction mechanism [33], (d) DLIT image of another monocrystalline cell taken at  $-5\text{ V}$ .

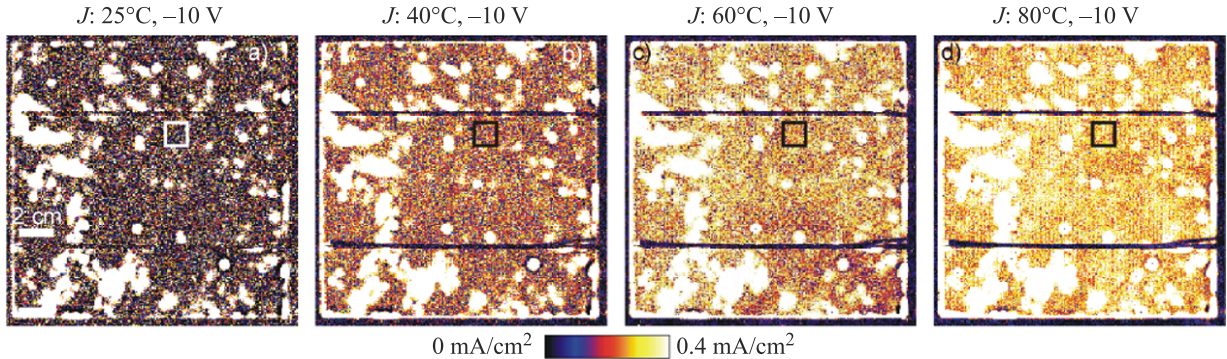


Fig. 12: DLIT-based current density images of a multicrystalline cell, measured at  $-10\text{ V}$  at different temperatures [55].

neous. Together with the edge current discussed above, it should be responsible for the positive temperature coefficient of the reverse current at low reverse bias, see next Section. In Fig. 12 also the edge current under reverse bias, which was discussed above, is clearly visible.

### 3.4. The reverse current

Since all junction breakdown or other conduction phenomena discussed in this Section appear far below the nominal breakdown voltage for a bulk doping concentration of  $10^{16}\text{ cm}^{-3}$  of about  $-60\text{ V}$  [4,30], they will be called in the following “pre-breakdown” phenomena. A review on the understanding of junction breakdown in multicrystalline silicon solar cells has been published recently [56], which was based on the state of the art in 2010. Therefore, this topic will only briefly be summarized here and updated by some most recent results. A general finding for most industrial multicrystalline cells is that, at low reverse bias (typically up to  $-3$  to  $-5\text{ V}$ , see also Fig. 3 (c), the reverse characteristics is linear, whereas at higher reverse bias the current increases more or less exponentially. As a rule, beyond a certain threshold voltage (typically about  $-13\text{ V}$  for a net doping concentration of  $10^{16}\text{ cm}^{-3}$ ) the steepness (slope) of the exponential characteristics further increases. Below this threshold voltage the temperature coefficient (TC) of the current is positive and beyond it becomes negative. These properties are nicely visible in Fig. 13 [55,56].

Detailed quantitative local investigations of pre-breakdown in multicrystalline cells have been performed by many authors using reverse-bias DLIT imaging, reverse-bias electroluminescence (ReBEL) imaging, and electron beam-induced current (EBIC) imaging methods. Generally, all pre-breakdown events appear locally in microscopically small positions. Only the conventional avalanche or Zener breakdown at a plane junction, which was discussed in Sect. 2, may lead to a homogeneous breakdown current. It has been found that local pre-breakdown sites in silicon solar cells can be classified into three types called type-1, type-2, and type-3 [56]. For a net doping concentration of about  $10^{16}\text{ cm}^{-3}$ , type-1 dominates up to  $-3\text{--}-5\text{ V}$ , type-2 dominates from  $-3\text{--}-5\text{ to }-13\text{ V}$ , and type-3 dominates beyond  $-13\text{ V}$ . Since all breakdown mechanisms are governed by

the electric field in the p-n junction, increasing the bulk doping concentration leads to a reduction of these voltage limits and vice versa. The net doping concentration in upgraded metallurgical grade (UMG) material is usually higher than the usual value of  $10^{16}\text{ cm}^{-3}$ , therefore, the reduction of the breakdown voltage in cells made from UMG material is due to the higher doping concentration there [57].

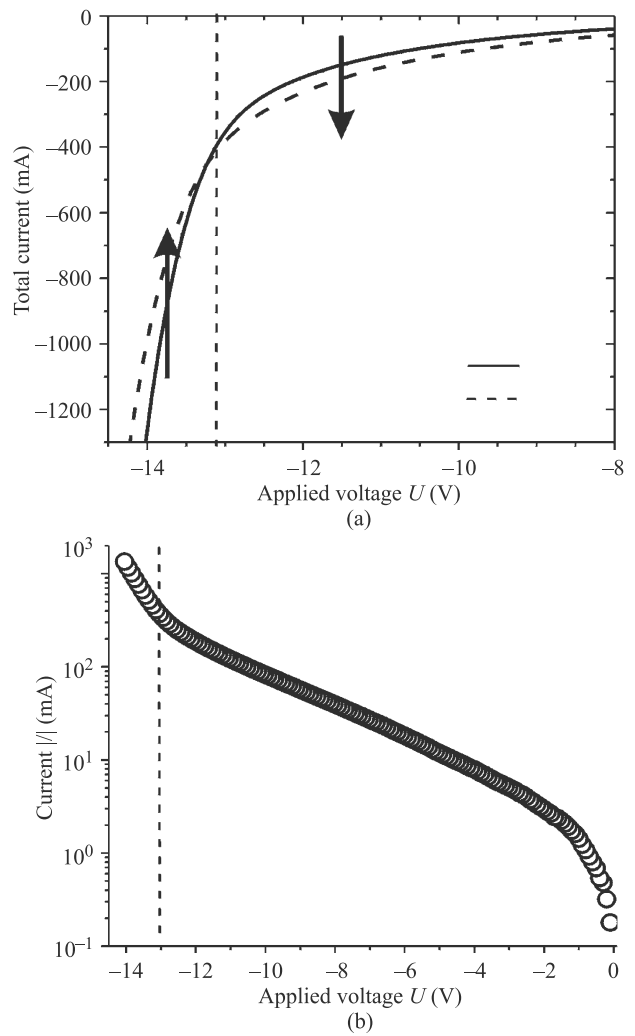


Fig. 13. (a) Reverse characteristics of a typical multicrystalline solar cell at two temperatures, (b) at room temperature in half-logarithmic drawing [55,56].

The type-1 breakdown, which also has been named “early breakdown”, corresponds to essentially ohmic current contributions. They are due to local ohmic shunts, like Al particles at the surface [58], and to the other ohmic conduction mechanisms discussed in the previous Section. Actually, ohmic conduction is no junction breakdown mechanism in the physical sense. Nevertheless, especially if conduction by Al particles is considered, these sites appear in DLIT like junction breakdown sites. They may even lead to light emission under reverse bias (ReBEL) [48,58], though there is only a poor correlation between the shunt strength and the amount of light emission [23]. This can be understood by considering that the light emission is essentially due to radiative intra-band thermalization of hot carriers, which are accelerated by high electric fields. Depending on the geometry of the shunt, which decisively governs the series resistance to it, and the shape of the current flow, an ohmic point shunt may or may not lead to sufficiently high local electric fields necessary for generating light emission.

The type-2 breakdown has also been named “defect-induced breakdown”, since it is always observed in the position of recombination-active grain boundaries [56]. Therefore, a good spatial correlation exists between the density of type-2 breakdown sites and the crystal defect density, which becomes visible, e.g., by forward bias electroluminescence imaging. It has also been found that the density of type-2 breakdown sites is significantly increased in cell regions, where the material has been facing to the walls of the silicon casting crucible [56]. It is well known that, during the silicon crystallization procedure, iron diffuses out of the casting crucible into the silicon material. Hence, it can be expected that iron may play a decisive role in forming these breakdown sites. Indeed, it had been shown in micro X-ray fluorescence investigations by Kwapil *et al.* [59] that iron-containing precipitates may exist in type-2 breakdown sites. By performing TEM investigations in these sites, needle-shaped FeSi<sub>2</sub> precipitates have recently been found in grain boundaries, which may stick through the p-n junction [60]. They consist from  $\alpha$ -type FeSi<sub>2</sub>, which is a quasi-metallic silicide modification. It can be assumed that this silicide forms a Schottky diode to the low-doped bulk material and an ohmic contact to the highly doped emitter. Figure 14 (a) shows a sketch of the proposed geometry of the type-2 breakdown sites [56]. The breakdown should occur at the lower end of the precipitate needle, where the field strength is highest due to the electrostatic tip effect. It will be shown below that, for a p-n junction, this tip effect reduces the breakdown voltage from -60 to -13 V. Even for a plane Schottky diode the reverse current mechanism differs considerably from that in a p-n junction [4]. Here the conduction mechanism is thermionic field emission, which is influenced by image-force effects and the field dependence of the barrier height. In Fig. 14(b) the mechanism of thermionic field emission is sketched for n-material. It is visible that the electrons may tunnel through the uppermost part of the energy barrier. Therefore, the reverse current in a Schottky barrier increases gradually with the reverse bias

and becomes significant already at lower field strength than that of a p-n junction. The temperature coefficient of this current is positive. It can be expected that the reverse current of a Schottky diode in a tip geometry of Fig. 14(a) also depends on geometrical parameters, like the inclination of the grain boundary and the remaining length of the precipitate needle in the bulk material. Moreover, it cannot be excluded that  $\alpha$ -FeSi<sub>2</sub> is not the only type of precipitates leading to type-2 breakdown sites. It was shown by Schneemann *et al.* [61] that indeed the onset voltages of different type-2 breakdown sites are different, and that the current through each site is series resistance-limited. Only the superposition of an ensemble of many breakdown sites with consecutive appearance of breakdown currents leads to the exponentially increasing reverse current observed for the whole cell.

The type-3 breakdown sites are responsible for the faster increasing exponential current contribution, which dominates for a doping concentration of  $10^{16} \text{ cm}^{-3}$  beyond -13 V and shows a negative temperature coefficient of the current. Only this current is due to the avalanche mechanism (impact ionization), which is theoretically expected to dominate the whole breakdown behaviour of silicon solar cells [4]. The reason for the unexpectedly low breakdown voltage is local field increase at a curved (bowl-shaped) p-n junction. It was calculated by Sze and Gibbons [30] that a bowl-shaped curvature of the junction with a radius of 300 nm reduces the breakdown voltage from -60 to -13 V. Solar cells with acidic texture (iso-texture), which is commonly used for

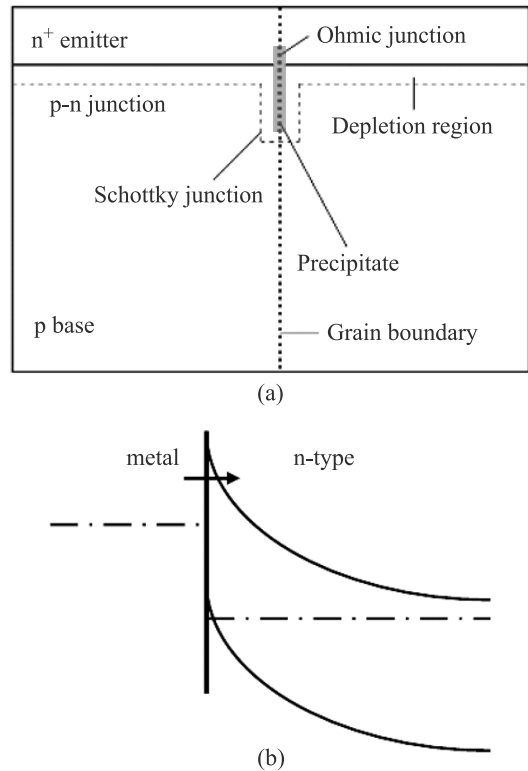


Fig. 14. (a) Proposed geometry of the type-2 breakdown sites [56],  
(b) thermionic breakdown mechanism.

multicrystalline cells, usually contain in certain regions a high density of several  $\mu\text{m}$  deep etch pits with sharp tips having a radius in the nm-range [62]. If the phosphorous diffusion leads to a junction depth of 300 nm below the surface, which is a typical value, at the tips of these etch pits the junction is bowl-shaped with a radius of 300 nm, which just explains the amount of the reduction of the breakdown voltage. In contrast to the type-2 breakdown sites, the onset voltages of all these type-3 breakdown sites in a cell are the same. Therefore, in spite of the fact that also these microscopic breakdown currents should be series resistance-limited, their simultaneous onset leads to a steep increase of the reverse current within a small reverse bias range, as shown in Fig. 13(b). It has been found that these etch pits are not caused by conventional bulk dislocations (their density in mc material is much higher than the density of these etch pits), but rather by special line defects lying in certain grain boundaries [63]. Nievendick *et al.* [64] have found a general correlation between breakdown voltage and the degree of roughness in acid etched cells, which should also be due to the curving of the p-n junction at a rough surface. In solar cells with alkaline texture no etch pits occur. Nevertheless, there is also avalanche breakdown in such cells, but the threshold voltage is some Volts higher than for acidic texture. It could be shown recently that in such cells preferential phosphorous diffusion in certain line defects in grain boundaries also lead to curved and partly bowl-shaped p-n junctions [65]. Here, due to geometrical reasons, the effective curvature radius under reverse bias is larger than for the deeper etch pits, which explains the higher breakdown voltage. It can be expected that this mechanism is active also for acidic textured solar cells, but there it should be covered by the dominating effect of the etch pits.

Thus, the pre-breakdown behaviour of multicrystalline cells is basically understood now. In monocrystalline cells there are no crystal defects and therefore also no etch pits, precipitates, and sites of preferred phosphorous diffusion. Of course, the ohmic conduction mechanisms, like Al particles or hopping conduction at the edge, are also active in monocrystalline cells. Indeed, the reverse currents of monocrystalline cells are, in the voltage range below  $-20$  V, one to two orders of magnitude lower than that of multicrystalline cells. As also Fig. 11 (d) shows, the local breakdown sites in monocrystalline cells are concentrated at the edges and below the busbars. Also in the edge regions some irregularities of the electric field may be expected, which may lead to avalanche-type pre-breakdown. In a recent work of Dubois *et al.* [66] breakdown on alkaline etched monocrystalline UMG cells of various doping concentrations has been investigated. It was found that the breakdown current shows a negative temperature coefficient in the whole investigated reverse bias regime. The “hard” breakdown voltages, where a steep increase of the reverse current occurs, coincide with empirical expressions obtained for uncompensated material. However, the negative temperature coefficient of the “soft” breakdown currents below these voltages is an indication that also here, most probably

in the edge regions, some electric field distortions exist leading to avalanche-type pre-breakdown.

Another possible reverse current mechanism, which is, e.g., used for interpreting reverse characteristics of infrared light detectors [67], is trap-assisted tunnelling. This mechanism is related to the hopping conduction discussed for low reverse biases in Sect. 3.4, except that here only one contributing level is considered. Like the internal field emission mechanism (Zener effect, band-to-band tunnelling), it should show a positive temperature coefficient of the current, since the gap energy shrinks with increasing temperature. The generally negative temperature coefficients measured in Ref. 66 indicate that trap-assisted tunnelling should not play a dominant role there. However, this does not mean that there are no local sites in mono- or multicrystalline cells where breakdown occurs by trap-assisted tunnelling.

### 3.5. Relation between dark and illuminated characteristics

In the two-diode model described by Eq. (2), current densities are used instead of currents. This makes the results independent of the cell area. However, it also implicitly assumes that the current density is homogeneous across the area. As we have seen in the previous Sections, this is as a rule not the case for industrial silicon solar cells. Another implicit assumption of this approach is the so-called “area-related series resistance”  $R_s$ , which is given here in units of  $\Omega \text{cm}^2$ . This means that each elementary region of the cell having an area of  $A$  is connected to the cell terminals by an independent series resistance  $R = R_s/A$ . In simplest case such a region is one pixel of an image of the cell. If, for example,  $2 \times 2$  pixel binning is applied, the pixel area  $A$  quadruples and  $R$  to each pixel quarters, but the area-related resistance  $R_s$  remains. The model behind this rule may be called “star model”, in which all elementary diodes are connected to one point, which is sketched in Fig. 15(a). Here one diode symbolizes the complete two-diode approach, including the first and second diode, a possible parallel resistance, and a possible photocurrent source, see Sect. 2. Until now, this star model is used in all concepts for imaging the local series resistance of solar cells, see Ref. 23.

In reality, a solar cell represents a three-dimensionally extended device implying both vertical and horizontal current paths. Here the series resistance to a certain region of the p-n junction may have different contributions, like the

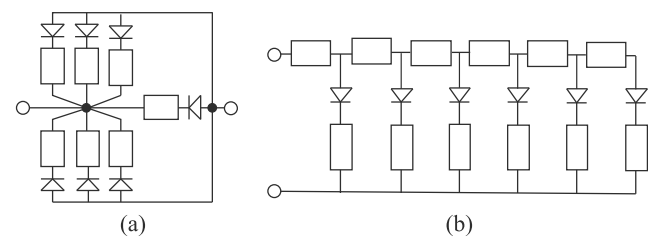


Fig. 15. (a) Star model of a solar cell, (b) distributed series resistance model.

contact resistances to the n- and the p-region, the series resistance within the bulk material, the series resistance within the emitter, and the resistances of the metallic busbars and grid lines. Most importantly, the current paths within such a device depend on the magnitude of the current and may be different between the dark and the illuminated case. Such a device can only be understood in detail by performing a 2- or 3-dimensional device simulation implying self-consistent solution of the transport and recombination equations, which leads to a consistent description of the dark and the illuminated characteristics [68]. Fortunately, the basic physical differences between the star model and a real solar cell can also be understood by applying a 1-dimensional model. Such a model neglects the thickness of the cell and describes e.g. the horizontal current flow from a grid line (assumed to have zero resistance) through the emitter to the region between two grid lines. For a full-area backside contact, as it is still standard in the present technology, the series resistances caused by the back contact and the bulk resistance are negligible. If we neglect also the series resistance to the busbars (4-wire contacting with multi-point contacts), the main contributions to the series resistance come from the resistance of the grid lines, from the contact resistance between the grid lines and the emitter, and from the sheet resistance in the emitter. The resistances of the emitter acts as a so-called “distributed series resistances” as sketched in Fig. 15(b), where again one diode symbolizes the first and second diode, a possible parallel resistance, and a possible photocurrent source. The resistances at the bottom will be discussed later. The essence of a distributed series resistance is a horizontal current flow in a resistive element with a continuous current drain on its whole current path. Then only the rightmost elementary series resistance in Fig. 15(b) carries only the current of its attached diode. From right to left, the elementary series resistances carry the currents of an increasing number of elementary diodes. This is a fundamentally different circuit than the star model of Fig. 15(a). In particular, this model cannot be described anymore by the area-related two-diode model of Eq. (2). Also the resistance of the grid lines may be described by such a distributed model, except that here the elementary diodes have to be replaced by another circuit of Fig. 15(b) describing the influence of the emitter resistance at a certain grid line position. Hence, in a real solar cell two circuits of this type are convoluted.

There have been numerous publications dealing with the influence of the distributed series resistance on solar cell characteristics, see, e.g., Refs. 69–71. These publications consider only a 1-dimensional series resistance, hence they assume that, e.g., the emitter sheet resistance represents the dominating contribution to the distributed series resistance. By discussing luminescence-based local series resistance images, we recently have concluded that in many cases the influence of the grid lines should be dominating over that of the emitter [71]. One important result of all these simulations is that, for low current densities, where the voltage drop at a distributed resistance is well below  $V_T$  (25.69 mV

at 25°C), the distributed resistance model is equivalent to the star model. Then, if the cell is homogeneous, the current flows still homogeneous and is not influenced by the series resistance yet. For a faultless solar cell this condition is met for current densities up to about 0.1  $J_{sc}$ . Hence, the differences between both models are limited to the high current part of the dark characteristics and to illuminated characteristics for illumination intensities above 0.1 suns. In Fig. 14(b), except of the distributed series resistance, for each elementary diode also an individual series resistance is introduced, which may be called a homogeneous (not distributed) series resistance [71]. This is an area-related resistance (which increases inverse to the area of the elementary diode) in the sense discussed above for Fig. 15(a), which may be e.g. due to a contact or path resistance.

It is well-known and was described, e.g., in Refs. 69–71 that the influence of a distributed series resistance may be modelled by considering current- and illumination intensity-dependent series resistances in a two-diode (star) model, hence for the whole cell assuming essentially homogeneous current flow. Though this is a very formal approach, it represents already an important improvement over the conventional two-diode model with a fixed series resistance. Recently an analytic approach has been published [71] for describing the current dependency of the effective series resistances of a whole device in the dark and under illumination, based on the equivalent circuit of Fig. 14 (b) and on the analytic results of [69]. This concept assumes that the whole considered cell can be described by a parallel acting set of equivalent circuits that can be described by the model in Fig. 14(b). The approach splits the series resistance into a homogeneous resistance  $R_{hom}$  (i.e., a non-distributed one) and a distributed resistance  $R_{dis}$ , both having the units of  $\Omega \text{ cm}^2$  and being fixed parameters. The effective (current-dependent) series resistance is a non-linear combination of  $R_{hom}$  and  $R_{dis}$ , which can be described in the dark and under illumination by two empirically obtained analytical equations. The procedure proposed in Ref. 71 first fits  $J_{01}$ ,  $J_{02}$ ,  $n_1$ ,  $n_2$ , and  $R_p$  to the low-current part of the dark characteristic, where the series resistance is just the sum of  $R_{hom}$  and  $R_{dis}$  and has only a weak influence. The ideality factor of the diffusion current  $n_1$ , which only weakly influences the shape of the dark characteristic, is chosen so that the measured open-circuit voltage matches the simulated one, see Sect. 3.2. These data allow the construction of the “suns- $V_{oc}$ ” dark characteristic also for higher currents, which is the characteristic without any series resistance. By comparing the high-current part of the measured dark characteristic with this suns- $V_{oc}$  characteristic, the current-dependent effective series resistance  $R_s(J)$  is obtained. By fitting this dependency to the distributed series resistance model, the values of  $R_{hom}$  and  $R_{dis}$  are obtained for this cell. It has turned out that the low-voltage part of the illuminated characteristic simulated by these data fits the measured one only for low illumination intensity. The reason for this will be discussed below. Therefore the values of  $n_2$ ,  $J_{02}$ , and (if

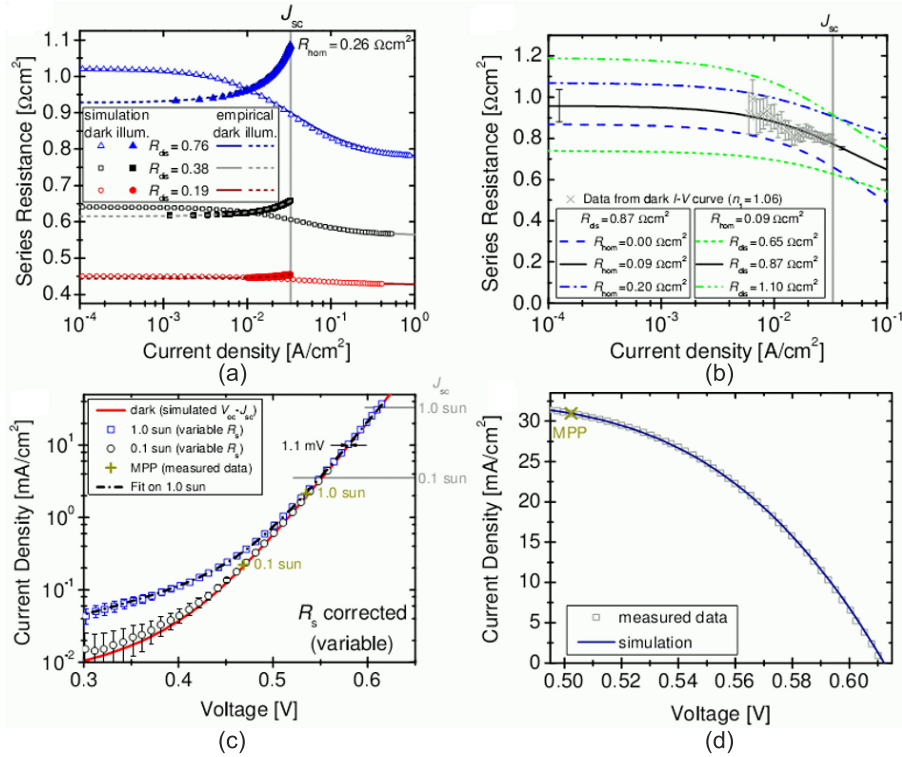


Fig. 16. (a) Simulation of the effective series resistance for various values of  $R_{hom}$  and  $R_{dis}$ , (b) example of fitting  $R_s(J)$  to  $R_{hom}$  and  $R_{dis}$ , (c) comparison of dark and reduced ( $J_{sc}$ -subtracted) illuminated characteristics, both  $R_s$ -corrected, (d) comparison measured and simulated illuminated characteristics near the maximum power point (all after [71]).

necessary) also  $R_p$  for the illuminated characteristic are fitted independently, based on the values of  $J_{01}$ ,  $n_1$ ,  $R_{hom}$ , and  $R_{dis}$  obtained from the evaluation of the dark characteristic.

Figure 16(a) shows typical results of the simulation for an illumination intensity of 1 sun. It is visible that the effective series resistances for low currents are independent of the current, but the distributed series resistance leads to a difference between the dark and the illuminated resistances. For increasing current, the dark resistance reduces, but the illuminated one increases. All these effects are due to certain current-dependent changes of the current paths in the device. Fig. 16(b) shows an example of fitting experimental  $R_s$  data to the theory of [71]. The final fitting parameters were  $R_{hom} = 0.09 \Omega \text{ cm}^2$ ,  $R_{dis} = 0.87 \Omega \text{ cm}^2$ ,  $R_p = 44.4 \text{ k}\Omega \text{ cm}^2$ ,  $J_{02} = 5.17 \times 10^{-8} \text{ A/cm}^2$  and  $n_2 = 2.76$ . The cell used for this example is the one also used for the experimental characteristic of Fig. 3. Figure 16(c) shows the comparison of the dark and the reduced (i.e.,  $J_{sc}$ -subtracted) measured and simulated illuminated characteristic (all  $R_s$ -corrected) for illumination intensities of 1 sun and 0.1 sun. We see that the illuminated characteristic can only be described by the data of the dark characteristic for 0.1 sun intensity, but not for 1 sun. Possible reasons for this will be discussed below. If the parameters  $J_{02}$  and  $n_2$  of the illuminated characteristic at 1 sun are fitted independently by using the values of  $J_{01}$ ,  $n_1$ ,  $R_{hom}$ , and  $R_{dis}$  of the dark characteristic, a perfect fit of the illuminated characteristic may be obtained, as Figs. 16(c) and (d) show [71]. A reasonable fit is also possible by

assuming constant series resistances, but then different values for them and for  $J_{01}$  have to be assumed in the dark and under illumination. It has to be mentioned that this method [71] is only accurate if the investigated cell is macroscopically homogeneous and faultless, hence if it does not show strong local inhomogeneities of the dark current (esp. of  $J_{01}$ ) and of the series resistance (no non-contacted regions).

The physical reason for the deviating values of  $J_{02}$ ,  $n_2$ , and, in certain cases, probably also of  $R_p$ , between the dark and the illuminated condition is a departure from the superposition principle, that has been described by Robinson *et al.* [72]. These authors pointed out that actually the semiconductor device equations are highly nonlinear with respect to carrier concentrations. Only the application of certain usual approximations, especially the total depletion approximation, leads to linearity, which is, e.g., a condition that the quasi Fermi levels cross the depletion region horizontally also under current flow. By performing PC1D simulations [73], which do not use such approximations, two types of departure from the superposition principle have been identified. Departure 1 only appears if the recombination levels have a strongly different capture cross section for electrons and holes, as it is the case, e.g., for an oxidized surface [41]. In this case the  $J_{sc}$ -reduced illuminated current is lying below the dark current for the same voltage. Departure 2 has been found in all simulations to varying degrees and is strongest for a low bulk lifetime. It leads, for low voltages, to a  $J_{sc}$ -reduced illuminated current higher than the dark current, as it

was shown in Fig. 16 (c). As shown there, the amount of this departure increases with increasing illumination intensity. Since this effect is only active at low voltages, it can be described as an extra (light intensity-dependent) contribution to the recombination (second diode) current or, in extreme cases, to an apparent reduction of  $R_p$  in the illuminated characteristics. The deeper physical reason for both departures is the fact that, under illumination and under current flow, the electron quasi Fermi level in the bulk is lying above that at the same p-n junction voltage in the dark. This leads to an earlier saturation of recombination via saturable SRH-defects (departure 1) and to a generally higher bulk recombination level under illumination and low forward bias than in the dark (departure 2). Hence, the extra current being responsible for departure 2 is due to recombination in the bulk and not in the depletion region. Describing it in the two-diode model as another contribution to the (depletion region) recombination current is only a formal measure. In reality, this is a variation of the first diode (diffusion) current, which is due to recombination in the bulk. Note that this effect is the reason why, for quantitative photoluminescence (PL) image evaluation, always a PL image taken under short-circuit condition has to be subtracted from all other PL images [74].

It has been reported sometimes that the parallel resistance  $R_p$  of a solar cell depends on the illumination intensity [75]. If the parallel resistance is measured as the inverse of the slope of the dark or illuminated characteristics at 0 V (which is actually wrong even for homogeneous cells, see discussion of Eq. (7) in Sect. 2), this “effective” parallel resistance sometimes reduces with increasing illumination intensity. Also cases have been reported where  $R_p$  increases with increasing light intensity [76]. According to Sect. 3.3 there is no known mechanism leading to an illumination-dependent parallel resistance. However, this effect may stem from a departure from the superposition principle like the one discussed in Ref. 72. In this work also other departures from the superposition principle are discussed, like the above mentioned distributed series resistance effect, high-injection conditions in the bulk, and voltage-dependent depletion region recombination, which may play a big role for thin-film solar cells, where the bulk is not thick compared to the depletion region anymore. A significant departure from the superposition principle, which is physically related to the distributed series resistance, was mentioned by Bowden and Rohatgi [77]. If there is an extended high-resistance region in a solar cell, where, e.g., the grid contact resistance is too high, this region is connected to the rest of the cell by a resistance. Also then the illuminated characteristic may show the characteristic “inclined roof”, which is usually interpreted as a parallel resistance. This effect, like departure 2 described by Robinson *et al.* [72], is proportional to the illumination intensity and vanishes for low intensity or in the dark. Also the effect reported in Ref. 75 was finally attributed to a high-resistive area [78]. The effect described in Ref. 76 may be due to the fact that, in this work, only the 1-diode model according to Eq. (3) and the approximation of a constant resistance was used. Nevertheless, this effect may exist. The application of the DLIT-

-based local efficiency analysis [22] to a typical industrial solar cell (implying an EL- (RESI)-based  $R_s$  image), and the analysis of the simulated global characteristics only by the slope at 0 V, lead to values of  $R_p^{dark} = 4.18 \text{ k}\Omega \text{ cm}^2$ ,  $R_p^{0.1sun} = 4.13 \text{ k}\Omega \text{ cm}^2$ , and  $R_p^{1sun} = 3.94 \text{ k}\Omega \text{ cm}^2$ , which is a measurable reduction. This analysis does not take into account any departure from the superposition principle after Robinson *et al.* [72] but only local series resistance effects based on the two-diode model.

A possible explanation of this effect will be described here for the first time. It was mentioned already for the discussion of Eq. (7) in Sect. 2 that the slope of the  $I$ - $V$  characteristics close to 0 V is significantly influenced by  $J_{02}$  and  $n_2$  and may be responsible for the effective parallel resistance of a cell. It was also described in Sect. 3.1 that  $J_{02}$  is flowing only in some local positions where the p-n junction is crossed by extended defects. This may be the edge of the cell, where the local series resistance is especially high. In the dark, a  $J_{02}$ -type edge shunt shows a differential resistance at 0 V given by Eq. (7). Under illumination and under short-circuit of the busbars, however, due to the series resistance to this shunt, such a region may be forward-biased by about 100 mV. Under this forward bias the differential resistance of a  $J_{02}$ -shunt is significantly reduced due to its exponential characteristics, which leads to a reduced effective parallel resistance of the whole device under illumination, compared to the dark case. It must be evaluated by further measurements and simulations, whether this effect is strong enough for explaining measured illumination-induced parallel resistances.

## 4. Summary and outlook

This review article summarizes a number of findings on industrial mono- and multicrystalline silicon solar cells, which have been obtained only in the last years and are not yet contained in any textbooks on semiconductor device physics [4] or solar cell physics and technology [11,12]. Nevertheless, they strongly influence the electronic properties of industrial solar cells and have to be understood for further optimizing their efficiency. These results were only described in the original literature and are collected for the first time in this review. The most important findings may be summarized as follows:

1. The depletion region recombination (second diode) current does not flow homogeneous but only in local positions, where extended recombination-active defects cross the p-n junction. This may be the edge of the cell, scratches, or some other still unidentified defects.
2. The main reason for the large ideality factor of the recombination current is most probably multi-level recombination. This recombination type is only effective for extended defects, showing a very high local density of deep states.
3. The same type of defects is a source of ohmic currents under weak reverse bias by hopping conduction. Other important ohmic current sources are Al particles at the surface, cracks, incompletely opened edge, and SiC fila-

- ments in multicrystalline material. There are indications that there is another still unidentified weak homogeneous current flow in multicrystalline cells, also showing a positive temperature coefficient.
4. Since the surface of the p-type bulk in the edge region is expected to be depleted, preferred electron injection from the emitter into this potential groove leads to a spatial extension of the region of edge recombination, which may significantly increase the amount of edge recombination and also may lead to ideality factors larger than two.
  5. The ideality factor of the diffusion (first diode) current may be larger than unity due to recombination saturation effects.
  6. In multicrystalline material, grain boundaries may significantly contribute to the diffusion current.
  7. The pre-breakdown behaviour of the cells is governed by microscopically small local breakdown sites. Until now three basically different breakdown types were identified, which are type-1 (early breakdown, ohmic or nearly ohmic, mostly by Al particles, see finding 3), type-2 (defect-induced breakdown, always in recombination-active grain boundaries, caused by FeSi<sub>2</sub> needles or other precipitates), and type-3 (avalanche breakdown, local field increase by etch pits or by preferential phosphorous diffusion at line defects in grain boundaries).
  8. The two-diode model, even if a series and a parallel resistance are included and if variable ideality factors are regarded, is only a coarse approximation of a solar cell, which only holds correct for low current densities. For current densities higher than 0.1  $J_{sc}$ , the influence of the distributed series resistance has to be regarded. This effect leads to changes of the current paths between dark and illumination and for different currents.
  9. This distributed series resistance can approximately be regarded as a current-dependent effective (lumped) series resistance, which can be given analytically as a function of current, different for the dark and illuminated case, and requires the introduction of only one new parameter ( $R_{dis}$ ).
  10. The first diode current under illumination deviates from that in the dark due to a known deviation from the superposition principle. Though this additional current contribution has some similarity to the depletion region recombination current, it is caused by recombination in the bulk.
- This article only deals with results obtained on solar cells of the presently dominating technology, which includes p-base material, full area Al back contact, P-diffused emitter, and screen-printed contacts. However, even if future novel concepts like n-base material, dielectric backside passivation with local contacts, or selective emitters are employed, the basic sources of non-ideal behaviour described here will remain as described, even for mono-crystalline material, where applicable. Some physical questions still remain open for coming investigations, which are, e.g.:
- Which crystal defects, except the edge and scratches, are responsible for the depletion region recombination current? How is their correlation to the recombination-active bulk crystal defects?
  - Which other defects, except FeSi<sub>2</sub> needles, are responsible for type-2 breakdown?
  - What is the origin of the homogeneous reverse current observed in multicrystalline cells?

## Acknowledgements

This article is based on an invited lecture of the author at the “Silicon Forest” workshop 2012 in Falkau, Germany. The author is grateful to S. Glunz (Fraunhofer ISE, Freiburg) and J. Schmidt (ISFH, Hameln) for inviting him to this lecture. Many of the results introduced here were obtained with financial support by the German Federal Ministry for the Environment, Nature Conservation and Nuclear Safety and by industry partners within the research cluster “SolarWinS” (contract No. 0325270C) and its preceding projects. The cooperation with all colleagues in these projects is gratefully acknowledged. This regards especially my previous and present colleagues at MPI Halle M. Langenkamp (now with FMC Technologies, Kongsberg), I. Konovalov (now with University of Applied Sciences Jena), J.-P. Rakotonianina (now with Silicor Materials), J.-M. Wagner (now with Kiel University), J. Bauer, A. Haehnel, and S. Rißland (all MPI Halle). Many thanks to H. Leipner (Halle University) for performing the scratching experiments, to P.P. Altermatt and S. Steingrube (both Hannover University) for performing simulations, and to S. Glunz (Fraunhofer ISE, Freiburg) for providing cells for the scratching experiments. Many thanks to P.P. Altermatt and J. Bauer for valuable discussions to this article.

## References

1. G. Hering, “Das Jahr des Drachen”, *Photon* **4**, 42–63 (2012). (in German)
2. [http://en.wikipedia.org/wiki/Solar\\_cell#History\\_of\\_solar\\_cells](http://en.wikipedia.org/wiki/Solar_cell#History_of_solar_cells).
3. M.A. Green, K. Emery, Y. Hishikawa, W. Warta, and E.D. Dunlop, “Solar cell efficiency tables (version 39)”, *Prog. Photovolt: Res. Appl.* **20**, 12–20 (2012).
4. S.M. Sze and K.K. Ng, *Physics of Semiconductor Devices*, Wiley-Interscience, Hoboken, 2007.
5. A. Müller, M. Ghosh, R. Sonnenschein, and P. Woiditsch, “Silicon for photovoltaic applications”, *Mater. Sci. Eng. B* **134**, 257–262 (2006).
6. H.J. Queisser, “Forward characteristics and efficiencies of silicon solar cells”, *Solid State Electron.* **5**, 1–10 (1962).
7. A. Kaminski, J.J. Marchand, H. El Omari, A. Laugier, Q.N. Le, and D. Sarti, “Conduction processes in silicon materials”, *Proc. 25<sup>th</sup> IEEE Phot. Spec. Conf.*, pp. 573–576, Washington DC, 1996.
8. A. Schenk and U. Krumbein, “Coupled defect-level recombination: Theory and application to anomalous diode characteristics”, *J. Appl. Phys.* **78**, 3185–3192 (1995).
9. K.R. McIntosh, “Lumps, humps and bumps: Three detrimental effects in the current-voltage curve of silicon solar cells”, *Ph.D. Thesis*, University of New South Wales, Sydney, 2001.
10. A.S.H. van der Heide, A. Schönecker, J.H. Bultman, and W.C. Sinke, “Explanation of high solar cell diode factors by nonuniform contact resistance”, *Prog. Photovolt: Res. Appl.* **13**, 3–16 (2005).

11. M.A. Green, *Solar Cells – Operating Principles, Technology And System Applications*, UNSW, Sydney 1998.
12. P. Würfel, *Physics Of Solar Cells – From Principles To New Concept*, Wiley, Weinheim, 2005.
13. A. Simo and S. Martinuzzi, “Hot spots and heavily dislocated regions in multicrystalline silicon cells”, *Proc. 21<sup>st</sup> IEEE Phot. Spec. Conf.*, pp. 800–805, Kissimee, USA, 1990.
14. O. Breitenstein, W. Eberhardt, and K. Iwig, “Imaging the local forward current density of solar cells by dynamical precision contact thermography”, *Proc. 1<sup>st</sup> World Conf. on Photovoltaic Energy Conversion*, pp. 1633–1836, Waikaloa, Hawaii, 1994.
15. O. Breitenstein, K. Iwig, and I. Konovalov, “Evaluation of local electrical parameters of solar cells by dynamic (lock-in) thermography”, *Phys. Status Solidi A* **160**, 271–282 (1997).
16. P.K. Kuo, T. Ahmed, H. Jin, and R.L. Thomas, “Phase-locked image acquisition in thermography”, *Proc. SPIE* **1004**, 41–45 (1988).
17. G. Busse, D. Wu, and W. Karpen, “Thermal wave imaging with phase sensitive modulated thermography”, *J. Appl. Phys.* **71**, 3962–2965 (1992).
18. O. Breitenstein, M. Langenkamp, F. Altmann, and D. Katzer, “Microscopic lock-in thermography investigations of leakage sites in integrated circuits”, *Rev. Sci. Instr.* **71**, 4155–4160 (2000).
19. O. Breitenstein, M. Langenkamp, O. Lang, and A. Schirrmacher, “Shunts due to laser scribing of solar cells evaluated by highly sensitive lock-in thermography”, *Sol. Energ. Mat. Sol. C.* **65**, 55–62 (2001).
20. O. Breitenstein, W. Warta, and M. Langenkamp, *Lock-in Thermography – Basics and Use for Evaluating Electronic Devices and Materials* (second edition), Springer, Heidelberg/New York 2010.
21. Breitenstein, “Nondestructive local analysis of current-voltage characteristics of solar cells by lock-in thermography”, *Sol. Energ. Mat. Sol. C.* **95**, 2933–2936 (2011).
22. O. Breitenstein, “Local efficiency analysis of solar cells based on lock-in thermography”, *Sol. Energ. Mat. Sol. C.* **107**, 381–389 (2012).
23. O. Breitenstein, J. Bauer, K. Bothe, D. Hinken, J. Müller, W. Kwapił, M.C. Schubert, and W. Warta, “Can luminescence imaging replace lock-in thermography on solar cells?”, *IEEE J. Photovoltaics* **1**, 159–167 (2011).
24. W. Shockley, “The theory of p-n junctions in semiconductors and p-n junction transistors”, *Bell Syst. Tec. J.* **28**, 435–489 (1949).
25. C.T. Sah, R.N. Noice, W. Shockley, “Carrier generation and recombination in p-n junctions and p-n junction characteristics”, *Proc. IRE* **45**, 1228–1243 (1957).
26. <http://pveducation.org/pvcdrom>
27. O. Breitenstein and J.-P. Rakotonaina, “Electrothermal simulation of a defect in a solar cell”, *J. Appl. Phys.* **97**, 074905 (2005).
28. K.R. McIntosh, P.P. Altermatt, and G. Heiser, “Depletion-region recombination in silicon solar cells: When does  $m_{dr} = 2?$ ”, *Proc. 16<sup>th</sup> Eur. Phot. Solar Energy Conf.*, pp. 251–254, Glasgow, 2000.
29. S.L. Miller, “Ionization rates for holes and electrons in silicon”, *Physical Review* **105**, 1246–1249 (1957).
30. S.M. Sze and G. Gibbons, “Effect of junction curvature on breakdown voltage in semiconductors”, *Solid State Electron.* **9**, 831–845 (1966).
31. O. Breitenstein and J. Heydenreich, “Non-ideal I-V characteristics of block-cast silicon solar cells”, *Solid-State Phenomena* **37–38**, 139–144 (1994).
32. M. Hermle, J. Dicker, W. Warta, S.W. Glunz, and G. Willeke, “Analysis of edge recombination for high-efficiency solar cells at low illumination densities”, *Proc. 3<sup>rd</sup> World Conf. Phot. Energ. Conversion*, pp. 1009–1012, Osaka, 2003.
33. O. Breitenstein, P. Altermatt, K. Ramspeck, M.A. Green, J. Zhao, and A. Schenk, “Interpretation of commonly observed I-V characteristics of c-Si cells having ideality factors larger than two”, *Proc. 4<sup>th</sup> World Conf. Phot. Energ. Conversion*, pp. 789–884, Waikaloa, Hawaii 2006.
34. O. Breitenstein, P. Altermatt, K. Ramspeck, and A. Schenk, “The origin of ideality factors  $n > 2$  of shunts and surfaces in the dark I-V curves of Si solar cells”, *Proc. 21<sup>st</sup> Eur. Phot. Solar Energ. Conf.*, pp. 652–628, Dresden, 2006.
35. S. Steingrube, O. Breitenstein, K. Ramspeck, S. Glunz, A. Schenk, and P.P. Altermatt, “Explanation of commonly observed shunt currents in c-Si solar cells by means of recombination statistics beyond the Shockley-Read-Hall approximation”, *J. Appl. Phys.* **110**, 014515 (2011).
36. R. Kühn, P. Fath, and E. Bucher, “Effects of pn-junction bordering on surfaces investigated by means of 2D-modeling”, *Proc. 28<sup>th</sup> IEEE Phot. Special. Conf.*, pp. 116–119, Anchorage, 2000.
37. M. Nardone, V.G. Karpov, D. Shvydka, and M.L.C. Attygalle, “Theory of electronic transport in non-crystalline junctions”, *J. Appl. Phys.* **106**, 074503 (2009).
38. R.A. Sinton, “Predicting multi-crystalline solar cell efficiency from lifetime measured during cell fabrication” *Proc. 3<sup>rd</sup> World Conf. Phot. Energ. Conversion*, pp. 1028–1031, Osaka, 2003.
39. S. Rißland and O. Breitenstein, “High resolution saturation current density imaging at grain boundaries by lock-in thermography”, *Solar Energ. Mat. Sol. C.* **104**, 121–124 (2012).
40. D. Macdonald and A. Cuevas, “Reduced fill factors in multi-crystalline silicon solar cells due to injection-level dependent bulk recombination lifetimes”, *Prog. Photovolt: Res. Appl.* **8**, 363–375 (2000).
41. S.J. Robinson, S.R. Wenham, P.P. Altermatt, A.G. Aberle, G. Heiser, and M.A. Green, “Recombination rate saturation mechanisms at oxidized surfaces of high-efficiency solar cells”, *J. Appl. Phys.* **78**, 4740–4754 (1995).
42. W. Schröter, J. Kronewitz, U. Gnauert, F. Riedel, and M. Seibt, “Bandlike and localized states at extended defects in silicon”, *Phys. Rev.* **B52**, 13 726–13 729 (1995).
43. S. Dubois, O. Palais, M. Pasquinelli, S. Martinuzzi, C. Jausaud, and N. Rondel, “Influence of iron contamination on the performances of single-crystalline silicon solar cells: Computed and experimental results”, *J. Appl. Phys.* **100**, 024510 (2006).
44. S. Rißland and O. Breitenstein, “Evaluation of luminescence images of solar cells for injection-level dependent lifetimes”, *Sol. Energ. Mat. Sol. C.* **111**, 112–114 (2010).
45. P.J. Cousins and J.E. Cotter, “The influence of diffusion-induced dislocations on high-efficiency solar cells”, *IEEE T. Electron Devices* **53**, 457–464 (2006).
46. P.P. Altermatt, J.O. Schumacher, A. Cuevas, M.J. Kerr, S.W. Glunz, R.R. King, G. Heiser, and A. Schenk, “Numerical modelling of highly doped Si:P emitters based on Fermi-Dirac statistics and self-consistent material parameters”, *J. Appl. Phys.* **92**, 3187–3197 (2002).

47. C. Reichel, F. Granek, J. Benick, O. Schulz-Wittmann, and S.W. Glunz, "Comparison of emitter saturation current densities determined by injection-dependent lifetime spectroscopy in high and low injection regimes", *Prog. Photovolt: Res. Appl.* **20**, 21–30 (2012).
48. O. Breitenstein, J.P. Rakotoniaina, M.H. Al Rifai, and M. Werner, "Shunt types in crystalline silicon solar cells", *Prog. Photovolt: Res. Appl.* **12**, 529–538 (2004).
49. J.P. Rakotoniaina, O. Breitenstein, M. Werner, M.H. Al-Rifai, T. Buonassisi, M.D. Pickett, M. Ghosh, A. Müller, and N. Le Quang, "Distribution and formation of silicon carbide and silicon nitride precipitates in block-cast multicrystalline silicon", *Proc. 20<sup>th</sup> Eur. Phot. Solar Energ. Conf.*, pp. 773–776, Barcelona, 2005.
50. J. Bauer, O. Breitenstein, A. Lotnyk, and H. Blumtritt, "Investigations on different types of filaments in multi-crystalline silicon for solar cells", *Proc. 22<sup>nd</sup> Eur. Phot. Solar Energ. Conf.*, pp. 994–997, Milan, 2007.
51. J. Bauer, O. Breitenstein, and J.P. Rakotoniaina, "Electronic activity of SiC precipitates in multicrystalline solar silicon", *Phys. Status Solidi A* **204**, 2190–2195 (2007).
52. N.F. Mott, *Metal-Insulator Transitions*, Taylor & Francis, London 1990.
53. S.Y. Myong and K.S. Lim, "Universal single-phonon variable range hopping for inorganic semiconducting polycrystalline films", *Appl. Phys. Lett.* **88**, 222110 (2006).
54. J.-M. Wagner, J. Bauer, and O. Breitenstein, "Classification of pre-breakdown phenomena in multicrystalline silicon solar cells", *Proc. 24<sup>th</sup> Eur. Phot. Solar Energ. Conf.*, pp. 925–929, Hamburg, 2009.
55. J. Bauer, "The origins of non-ideal current-voltage characteristics of silicon solar cells", *Ph.D. Thesis*, Martin-Luther University Halle-Wittenberg, 2009, <http://digital.bibliothek.uni-halle.de/hs/content/titleinfo/474968>, available at Südwestdeutscher Verlag für Hochschulschriften, Saarbrücken (2012), ISBN 978-3-8381-2865-8.
56. O. Breitenstein, J. Bauer, K. Bothe, W. Kwapił, D. Lausch, U. Rau, J. Schmidt, M. Schneemann, M.C. Schubert, J.-M. Wagner, and W. Warta, "Understanding junction breakdown in multicrystalline solar cells", *J. Appl. Phys.* **109**, 071101 (2011).
57. W. Kwapił, M. Wagner, M.C. Schubert, and W. Warta, "High net doping concentration responsible for critical diode breakdown behaviour of upgraded metallurgical grade multicrystalline silicon solar cells", *J. Appl. Phys.* **108**, 023708 (2010).
58. D. Lausch, K. Petter, R. Bakowski, C. Czekalla, J. Lenzner, H. v. Wenckstern, and M. Grundmann, "Identification of pre-breakdown mechanism of silicon solar cells at low reverse voltages", *Appl. Phys. Lett.* **97**, 073506 (2010).
59. W. Kwapił, P. Gundel, M.C. Schubert, F.D. Heinz, W. Warta, E.R. Weber, A. Goetzberger, and G. Martinez-Criado, "Observation of metal precipitates at prebreakdown sites in multicrystalline silicon solar cells", *Appl. Phys. Lett.* **95**, 232113 (2009).
60. A. Hähnel, J. Bauer, H. Blumtritt, and O. Breitenstein, "Electron microscope verification of prebreakdown-inducing  $\alpha$ -FeSi<sub>2</sub> needles in multicrystalline silicon solar cells", *J. Appl. Phys.* **113**, 044505 (2013).
61. M. Schneemann, A. Helbig, T. Kirchartz, R. Carius, and U. Rau, "Reverse biased electroluminescence spectroscopy of crystalline solar cells with high spatial resolution", *Phys. Status Solidi A* **207**, 2597–2600 (2010).
62. J. Bauer, J.-M. Wagner, A. Lotnyk, H. Blumtritt, B. Lim, J. Schmidt, and O. Breitenstein, "Hot spots in multicrystalline silicon solar cells: avalanche breakdown due to etch pits", *Phys. Status Solidi RRL* **3**, 40–42 (2009).
63. O. Breitenstein, J. Bauer, J.-M. Wagner, N. Zakharov, H. Blumtritt, A. Lotnyk, M. Kasemann, W. Kwapił, and W. Warta, "Defect-induced breakdown in multicrystalline silicon solar cells", *IEEE T. Electron Devices* **57**, 2227–2234 (2010).
64. J. Nievendick, W. Kwapił, and J. Rentsch, "Influence of trench structures induced by texturization on the breakdown voltage of multicrystalline solar cells", *Proc. 37<sup>th</sup> IEEE Photovoltaic Specialists Conference*, pp. 2913–2917, Seattle, 2011.
65. J. Bauer, D. Lausch, H. Blumtritt, N. Zakharov, and O. Breitenstein, "Avalanche breakdown in multicrystalline solar cells due to preferred phosphorous diffusion at extended defects", *Prog. Photovolt: Res. Appl.*, DOI: 10.1002/pip.2220.
66. S. Dubois, J. Veirman, N. Enjalbert, and P. Scheiblin, "Hard breakdown mechanism of compensated p-type and n-type single-crystalline silicon solar cells", *Solid State Electron.* **76**, 36–39 (2012).
67. M.A. Kinch, "Electronic properties of HgCdTe", *J. Vac. Sci. Technol.* **21**, 215–219 (1982).
68. P.P. Altermatt, G. Heiser, A.G. Aberle, A. Wang, J. Zhao, S.J. Robinson, S. Bowden, and M.A. Green, "Spatially resolved analysis and minimization of resistive losses in high-efficiency Si solar cells", *Prog. Photovolt: Res. Appl.* **4**, 399–414 (1996).
69. G.L. Araújo, A. Cuevas, and J.M. Ruiz, "The effect of distributed series resistance on the dark and illuminated current-voltage characteristics of solar cells", *IEEE T. Electron Devices* **33**, 391–401 (1986).
70. B. Fischer, P. Fath, and E. Bucher, "Evaluation of solar cell J(V)-measurements with a distributed series resistance model", *Proc. 16<sup>th</sup> Eur. Photovoltaic Solar Energy Conf.*, pp. 1365–1368, Glasgow, 2000.
71. O. Breitenstein and S. Rißland, "A two-diode model regarding the distributed series resistance", *Sol. Energ. Mat. Sol. C.* **110**, 77–86 (2013).
72. S.J. Robinson, A.G. Aberle, and M.A. Green, "Departures from the principle of superposition in silicon solar cells", *J. Appl. Phys.* **76**, 7920–7930 (1994).
73. <http://www.pveducation.org/pvcdrom/characterisation/pc1d>
74. T. Trupke, E. Pink, R.A. Bardos, and M.D. Abbott, "Spatially resolved series resistance of silicon solar cells obtained from luminescence imaging", *Appl. Phys. Lett.* **90**, 093506 (2007).
75. A. Sugianto, B.S. Tjahjono, L. Mai, and S.R. Wenham, "Investigations of unusual shunting behaviour due to phototransistor effect in n-type aluminum-alloyed rear-junction solar cells", *Sol. Energ. Mat. Sol. C.* **93**, 1986–1993 (2009).
76. F. Khan, S.N. Singh, and M. Husain, "Effect of illumination on cell parameters of a silicon solar cell", *Sol. Energ. Mat. Sol. C.* **94**, 1473–1476 (2010).
77. S. Bowden and A. Rohatgi, "Rapid and accurate determination of series resistance and fill factor losses in industrial silicon solar cells", *Proc. 17<sup>th</sup> Eur. Phot. Solar Energ. Conf.*, pp. 1802–1805, Munich, 2001.
78. A. Sugianto, O. Breitenstein, B.S. Tjahjono, A. Lennon, L. Mai, and S.R. Wenham, "Impact of localized regions with very high series resistances on solar cell performance", *Prog. Photovolt: Res. Appl.* **20**, 452–462 (2012).